

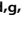




The NF- κ B Transcriptional Footprint Is Essential for SARS-CoV-2 Replication

 Benjamin E. Nilsson-Payant,^a  Skyler Uhl,^{a,b}  Adrien Grimont,^{d,h}  Ashley S. Doane,^{e,f}  Phillip Cohen,^{a,b}  Roosheel S. Patel,^{a,b}  Christina A. Higgins,^{a,b}  Joshua A. Acklin,^{a,b}  Yaron Bram,^c  Vasuretha Chandar,^c  Daniel Blanco-Melo,^a  Maryline Panis,^a  Jean K. Lim,^a  Olivier Elemento,^{e,f}  Robert E. Schwartz,^c  Brad R. Rosenberg,^a  Rohit Chandwani,^{d,g,h}  Benjamin R. tenOever^a

^aDepartment of Microbiology, Icahn School of Medicine at Mount Sinai, New York, New York, USA

^bGraduate School of Biomedical Sciences, Icahn School of Medicine at Mount Sinai, New York, New York, USA

^cDivision of Gastroenterology and Hepatology, Department of Medicine, Weill Cornell Medicine, New York, New York, USA

^dDepartment of Surgery, Weill Cornell Medicine, New York, New York, USA

^eDepartment of Physiology and Biophysics, Weill Cornell Medicine, New York, New York, USA

^fCaryl and Israel Englander Institute for Precision Medicine, Weill Cornell Medicine, New York, New York, USA

^gDepartment of Cell and Developmental Biology, Weill Cornell Medicine, New York, New York, USA

^hSandra and Edward Meyer Cancer Center, Weill Cornell Medicine, New York, New York, USA

Benjamin E. Nilsson-Payant and Skyler Uhl contributed equally to this work and share equal right to be listed as principal author. Author order was determined by coin flip.

ABSTRACT SARS-CoV-2, the etiological agent of COVID-19, is characterized by a delay in type I interferon (IFN-I)-mediated antiviral defenses alongside robust cytokine production. Here, we investigate the underlying molecular basis for this imbalance and implicate virus-mediated activation of NF- κ B in the absence of other canonical IFN-I-related transcription factors. Epigenetic and single-cell transcriptomic analyses show a selective NF- κ B signature that was most prominent in infected cells. Disruption of NF- κ B signaling through the silencing of the NF- κ B transcription factor p65 or p50 resulted in loss of virus replication that was rescued upon reconstitution. These findings could be further corroborated with the use of NF- κ B inhibitors, which reduced SARS-CoV-2 replication *in vitro*. These data suggest that the robust cytokine production in response to SARS-CoV-2, despite a diminished IFN-I response, is the product of a dependency on NF- κ B for viral replication.

IMPORTANCE The COVID-19 pandemic has caused significant mortality and morbidity around the world. Although effective vaccines have been developed, large parts of the world remain unvaccinated while new SARS-CoV-2 variants keep emerging. Furthermore, despite extensive efforts and large-scale drug screenings, no fully effective antiviral treatment options have been discovered yet. Therefore, it is of the utmost importance to gain a better understanding of essential factors driving SARS-CoV-2 replication to be able to develop novel approaches to target SARS-CoV-2 biology.

KEYWORDS NF- κ B, SARS-CoV-2

The cellular response to virus infection has evolved to encompass two defensive strategies, an immediate call to arms and a secondary call for reinforcements. The initial response generally focuses on the direct inhibition of virus replication by generating a cellular environment that is restrictive to high levels of transcription, translation, and cellular transport (1). This early response is largely coordinated by cytokines belonging to the type I interferon family (IFN-I) (2). IFN-I production is initiated following the detection of viral RNA and other pathogen-associated molecular patterns (PAMPs) (3). Members of the IFN-I family, most notably interferon β , are released into the extracellular milieu and can signal in both an autocrine and paracrine manner (4).

Citation Nilsson-Payant BE, Uhl S, Grimont A, Doane AS, Cohen P, Patel RS, Higgins CA, Acklin JA, Bram Y, Chandar V, Blanco-Melo D, Panis M, Lim JK, Elemento O, Schwartz RE, Rosenberg BR, Chandwani R, tenOever BR. 2021. The NF- κ B transcriptional footprint is essential for SARS-CoV-2 replication. *J Virol* 95: e01257-21. <https://doi.org/10.1128/JVI.01257-21>.

Editor Tom Gallagher, Loyola University Chicago

Copyright © 2021 American Society for Microbiology. All Rights Reserved.

Address correspondence to Rohit Chandwani, roc9045@med.cornell.edu, or Benjamin R. tenOever, Benjamin.tenOever@NYULangone.org.

Received 26 July 2021

Accepted 31 August 2021

Accepted manuscript posted online 15 September 2021

Published

IFN-I signaling results in the assembly of an additional transcription factor complex, termed interferon-stimulated gene factor 3 (ISGF3), which is responsible for the upregulation of ~200 antiviral genes collectively referred to as interferon-stimulated genes (ISGs) (5). Concomitant with this response, cellular detection of virus infection also induces a call for reinforcements. This strategy includes distinct classes of cytokines with chemoattractant properties called chemokines, which create biological gradients to attract immune cells involved in both innate and adaptive immunity (6, 7).

Cellular engagement of these two antiviral strategies relies largely on two families of transcription factors. Notably, the induction of IFN-I requires the concurrent activation of members of the interferon regulatory factors (i.e., IRF3 and IRF7) as well as NF- κ B transcription factor members (i.e., RelA/p65 and p50) (4, 8). Activation of these two pathways in response to virus infection is coordinated by pathogen recognition receptors (PRRs) that activate the IKK and IKK-related kinases (9). Direct phosphorylation of IRF3 and IRF7 by these kinases catalyzes their dimerization and association with histone acetyltransferases to induce gene transcription (10). In contrast to the IRFs, NF- κ B activation is induced indirectly by phosphorylation, which leads to degradation or cleavage of an inhibitor to enable nuclear translocation and transcriptional activation. Moreover, unlike the IRFs, NF- κ B activation is induced by many cellular stresses and is not restricted only to the engagement of PRR by viral infection (11).

The NF- κ B family consists of five members defined by so-called Rel homology domains and includes NF- κ B1 (p105/p50), NF- κ B2 (p100/p52), RelA (p65), RelB, and c-Rel (12). NF- κ B1 and NF- κ B2 are unique in this family, as they are synthesized as larger precursors, p105 and p100, that are posttranslationally processed to p50 and p52, respectively. Classical activation of NF- κ B is induced by the phosphorylation and subsequent degradation of I κ B α , an inhibitor of p50:p65 heterodimers that are retained in the cytoplasm as a result of I κ B α . Loss of I κ B α exposes a nuclear localization domain to enable their transport and transcriptional potential (13). Classical engagement of NF- κ B has been documented to be transient and activated by diverse stimuli, including cytokines, PAMPs, and damage-associated molecular patterns (DAMPs) (14). In contrast, nonclassical activation is slower, relying on *de novo* synthesis of NF- κ B inducing kinase (NIK), and occurs through processing of p105 directly, which associates with RelB and also induces the transcription of a wide array of cytokines (15). IRFs and the classical NF- κ B pathway cooperate to engage the IFN-I system, activating members of the STAT family (i.e., STAT1 and STAT2), which, along with IRF9, form the ISGF3 complex and induce hundreds of ISGs and, thus, enable the call to arms (16). In addition to this, NF- κ B alone can induce many proinflammatory cytokines and chemokines, thus initiating the call for reinforcements (11).

In general, viruses that cause human disease have evolved mechanisms to antagonize both defensive strategies described (17). Interestingly, it has been demonstrated that unlike many viral pathogens that infect humans, SARS-CoV-2 appears to selectively inhibit IFN-I signaling while allowing chemokine production to proceed mostly unabated (18). Numerous studies have now implicated a wide array of SARS-CoV-2 transcripts that participate in the suppression of the IFN-I response, including PRR-mediated activation of NF- κ B activation (19–24). Despite the antagonistic potential of SARS-CoV-2, here we show that infection culminates in NF- κ B activation, presumably mediated by one of the many cellular stress responses. Even though NF- κ B activation results in recruitment of the immune response, normally targeted by viruses, here we demonstrate that the transcriptional footprint of NF- κ B is essential for virus replication. Together, this series of events creates a cytokine-mediated inflammatory environment in the absence of a robust IFN-I response that culminates in the pathology associated with COVID-19.

RESULTS

Kinetics of early SARS-CoV-2 infection. To delineate the molecular basis for the imbalanced host response, we performed high-resolution kinetics of SARS-CoV-2 (USA-WA1/2020) infection in clonal human lung epithelial A549 cells stably expressing the

SARS-CoV-2 entry receptor ACE2 (25, 26). Poly(A)-enriched sequencing of total RNA extracts (here denoted RNA-seq) was performed at different multiplicities of infection (MOI) over a time course of 48 h postinfection (hpi). Differentially expressed genes (DEGs) indicated that the transcriptional response to SARS-CoV-2 infection was initiated at 8 hpi at an MOI of 1.0, whereas no discernible response was observed at lower MOIs at this time point (Fig. 1A). By 16 hpi, a robust host response was detected at all MOIs, which plateaued at the 36-hpi time point. Aligning this RNA-seq data to the genome of SARS-CoV-2 demonstrated that the host response to infection correlated with viral RNA levels (Fig. 1B). This also correlated with robust nucleocapsid (N) and spike (S) protein expression as detected by Western blot analysis (Fig. 1C). To gain a better sense of how viral load relates to the host response, we performed additional RNA-seq analyses on a more refined kinetics using a high MOI to ensure that all cells were infected and relatively synchronized (Fig. 1D). In agreement with our earlier studies, these data demonstrated that the transcriptional response to viral infection was initiated between 6 and 9 hpi, which persisted and steadily increased until 24 hpi (Fig. 1D).

Relative SARS-CoV-2 transcript abundance at each of these time points suggested that a significant host response to infection trails peak levels of virus replication by approximately 3 h at a high MOI (Fig. 1D and E). These data are distinct from RNA-seq profiles from environments in which only a subset of cells is infected, suggesting that many differentially expressed genes are derived from uninfected bystander events (Fig. 1A and B). This correlation between host response and viral reads was further corroborated by quantitative real-time PCR (qRT-PCR) for subgenomic nucleocapsid transcripts (sgN) and genomic envelope (E) viral RNA (Fig. 1F). Western blot analysis also corroborated robust production of nucleocapsid and the spike proteins beginning at 9 hpi (Fig. 1G). Furthermore, immunofluorescent staining for double-stranded RNA (dsRNA), a common PAMP generated in response to virus infection, demonstrated that SARS-CoV-2 produces significant amounts of this inflammatory RNA during the course of infection, in agreement with other independent studies (Fig. 1H) (27).

SARS-CoV-2 induces an early NF- κ B transcriptional signature. Gene set enrichment analyses (GSEA) of these data sets revealed that transcripts associated with tumor necrosis factor alpha (TNF- α) signaling via NF- κ B were the most upregulated starting at 9 hpi, remaining high for the duration of the infection (Fig. 2A). Consistent with prior results, we failed to observe a significant IFN-I signature despite robust induction of NF- κ B activity and inflammation. Examining enriched gene annotations, we observe the induction of both an inflammatory and an NF- κ B signature comprised of overlapping chemokines (e.g., *CXCL8*, *CXCL10*, *CXCL11*, and *CCL20*) in addition to proinflammatory cytokines such as *IL1A* and *IL-6* (Fig. 2B and C). In contrast to the induction of NF- κ B signaling and inflammation early in infection, a small subset of IFN-I-related genes did show modest transcriptional induction at the latest time point (Fig. 2D). RNA-seq data could be further validated by qRT-PCR, which showed upregulation of *NFKBIA* in the relative absence of an ISG response, as measured by *MX1* (Fig. 2E). Finally, Western blot analyses confirmed these results at a protein level, demonstrating a general lack of IFN-I engagement, as neither *MX1* expression nor phosphorylation of STAT1 or IRF3 was evident in response to SARS-CoV-2 (Fig. 2F). However, we did observe phosphorylation of $I\kappa B\alpha$, indicative of NF- κ B activation, as well as NF- κ B p65 itself, which is consistent with our RNA-seq data and gene enrichment predictions (Fig. 2F). Protein expression and secretion of proinflammatory cytokines, including *CXCL1*, *CXCL2*, *CXCL8*, *CCL2*, *CCL20*, and *IL-6*, into the cell culture media after SARS-CoV-2 infection was also confirmed by ELISA (Fig. 2G).

NF- κ B transcriptional signature dominates transcriptome of infected cells. To assess whether virus directly or indirectly activates NF- κ B signaling, we performed single-cell RNA sequencing (scRNA-seq) on A549-ACE2 cells, identifying infected and naive bystander cells based on the presence of multiple viral RNA transcripts (Fig. 3A and B). In agreement with what others have previously described, SARS-CoV-2 causes a significant reduction in host mRNAs, resulting in a large percentage of viral transcripts accounting for total RNA per infected cell (Fig. 3C) (28). Consistent with our previous

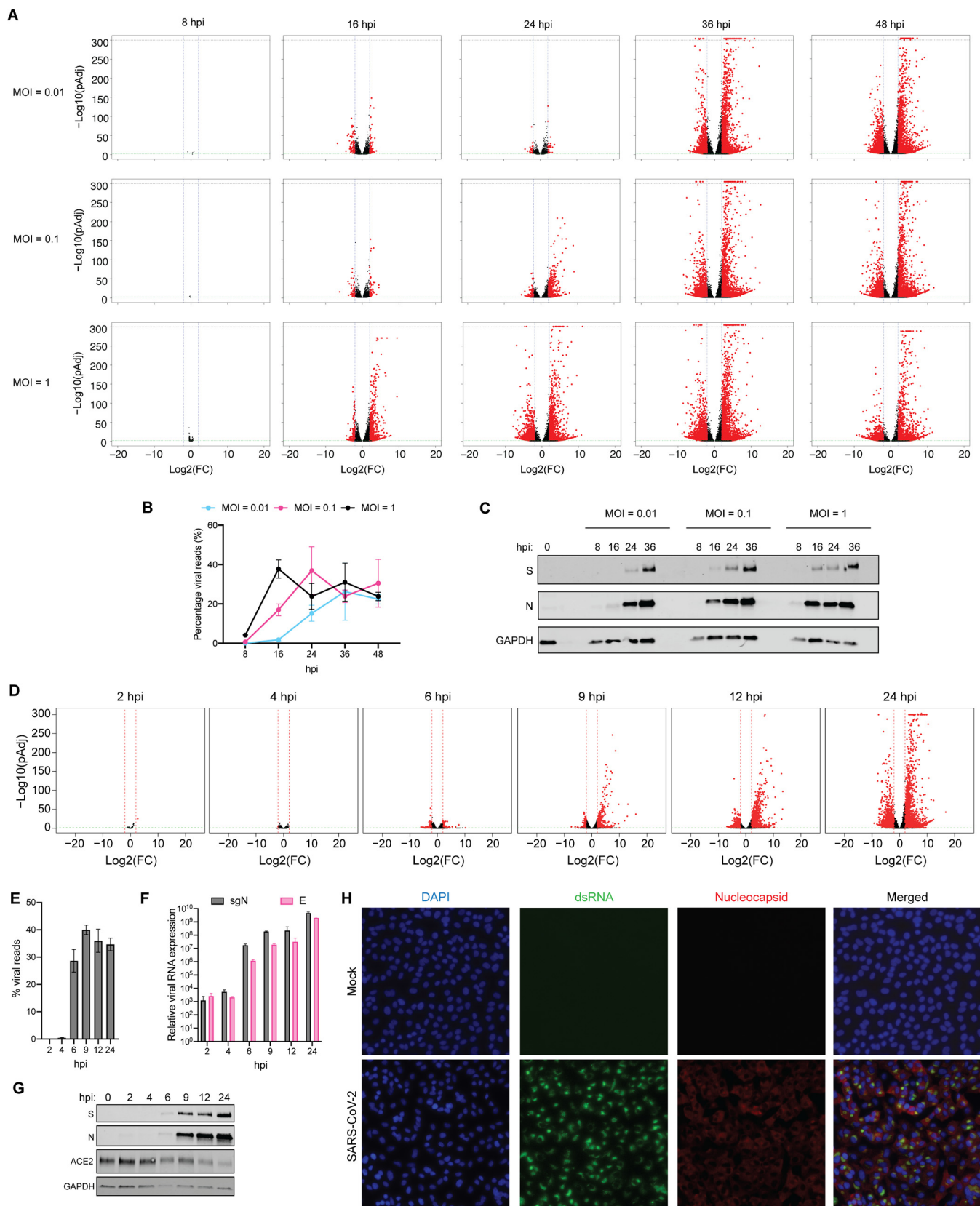


FIG 1 (A) Volcano plots depicting differentially expressed genes from RNA-seq analysis of A549-ACE2 cells infected with SARS-CoV-2 (MOI, 0.01/0.1/1) for the indicated amount of time compared to uninfected cells. Red dots indicate genes with a \log_2 (fold change) greater than 2 or less than -2 and an adjusted P value of less than 0.05. (B) Mean percentage of viral reads over total mapped reads in RNA-seq from SARS-CoV-2-infected A549-ACE2 cells. Error (Continued on next page)

observations, gene set enrichment testing comparing total unique molecular indices (UMIs) between infected and bystander cells revealed that transcripts associated with TNF- α signaling via NF- κ B were evident in both populations but dominated the transcriptome of infected cells (Fig. 3D and E). These data implicate NF- κ B signaling as the dominant driver of the host transcriptional response in virus-infected cells and a likely contributor to the underlying inflammation observed in COVID-19.

NF- κ B activation shapes the host response in SARS-CoV-2-infected cells. To better understand how the host response to SARS-CoV-2 is orchestrated at the transcriptional level, we next analyzed the epigenetic status of the cell in response to virus infection. To this end, assay for transposase-accessible chromatin with high-throughput sequencing (ATAC-seq) was performed on mock- and SARS-CoV-2-infected A549-ACE2 cells. We observed chromatin opening at most NF- κ B signaling targets, including *CXCL2*, *NFKBIA*, and *TNF* loci (Fig. 4A). In response to infection, the chromatin landscape was most altered by infection in the range of 20 to 200 kb from a given transcriptional start site (TSS) rather than at promoters, suggesting dynamic accessibility of regulatory elements (Fig. 4B). Indeed, newly accessible (SARS-CoV2 opening) and inaccessible (SARS-CoV2 closing) sites were enriched for chromatin locations that, based on A549 ENCODE data, corresponded to known poised (H3K4me¹ H3K27ac⁻) and active (H3K4me¹ H3K27ac⁺) enhancers, respectively (Fig. 4C to E). These data suggest that the response to SARS-CoV-2 infection is to repress normally active enhancers while activating enhancers that are normally poised.

Interestingly, when we examined motifs enriched among opening sites, there was a profound enrichment of the NF- κ B-related DNA-binding motifs for REL, NFKB1, and RELA but not for IRF3 or IRF7, which would otherwise be associated with an antiviral response (Fig. 4F). Consistent with this, our ATAC-seq showed that the greatest increase in genomic accessibility correlated with binding sites for members of the NF- κ B family (i.e., REL, RELA, RELB, NFKB1, and NFKB2), while the greatest decrease in accessibility correlated with binding sites for transcription factors of the TEAD signaling pathway (Fig. 4G). These alterations in enhancer sites corresponded to a transcriptional impact as measured by RNA-seq (Fig. 4H). Most notably, in our ATAC-seq data we detected in these dynamics a dramatic enrichment of TNF- α /NF- κ B-associated genes and associated enhancers to the exclusion of IFN-I signatures (Fig. 4I to K), in keeping with our earlier findings in the transcriptional dynamics associated with SARS-CoV-2 infection. Furthermore, enhancers belonging to these NF- κ B-inducible genes were among those displaying the greatest dynamics in chromatin accessibility (Fig. 4L).

NF- κ B is essential for SARS-CoV-2 biology. To determine the interplay between NF- κ B signaling and SARS-CoV-2 infection, we next silenced RelA (p65) or NF- κ B1 (p105/p50) and assessed the impact on virus-host dynamics. Surprisingly, we observed that diminished RelA expression correlated with a significant decrease in viral nucleocapsid protein levels (Fig. 5A). Moreover, silencing of NF- κ B1 resulted in a complete loss of detectable nucleocapsid levels comparable to targeting viral subgenomic nucleocapsid transcripts itself (Fig. 5A). This inhibition of viral replication, as measured by viral protein expression, following short interfering RNA-mediated silencing of RelA or NF- κ B1 was further confirmed by quantification of cells expressing nucleocapsid protein, as measured by immunofluorescence staining, showing significant loss of infected cells following targeting of NF- κ B1, RelA, or nucleocapsid directly (Fig. 5B). To ensure

FIG 1 Legend (Continued)

bars represent the standard deviations from three independent biological replicates. (C) Western blot analysis for SARS-CoV-2 spike (S) and nucleocapsid (N) as well as human GAPDH of whole-cell lysates from A549-ACE2 cells infected with SARS-CoV-2. (D) Volcano plots depicting differentially expressed genes from RNA-seq analysis of A549-ACE2 cells infected with SARS-CoV-2 (MOI, 2) for the indicated amount of time compared to uninfected cells. The red lines mark a \log_2 (fold change) greater than 2 or less than -2. The green lines mark an adjusted *P* value of less than 0.05. (E) Mean percentage of viral reads over total mapped reads in RNA-seq from SARS-CoV-2-infected A549-ACE2 cells (MOI, 2). (F) qRT-PCR analysis of A549-ACE2 cells infected with SARS-CoV-2 (MOI, 2). The graph depicts the relative mean accumulation of SARS-CoV-2 envelope genomic RNA (E) and nucleocapsid subgenomic RNA (sgN) normalized to human β -actin mRNA levels (*n* = 3). (G) Western blot analysis for SARS-CoV-2 spike (S) and nucleocapsid (N) as well as human ACE2 and GAPDH of whole-cell lysates from A549-ACE2 cells infected with SARS-CoV-2 (MOI, 2). (H) Immunofluorescence microscopy of A549-ACE2 cells infected with SARS-CoV-2 (MOI, 1, 24 hpi). Cells were stained for dsRNA, nucleocapsid, and nuclear DNA.

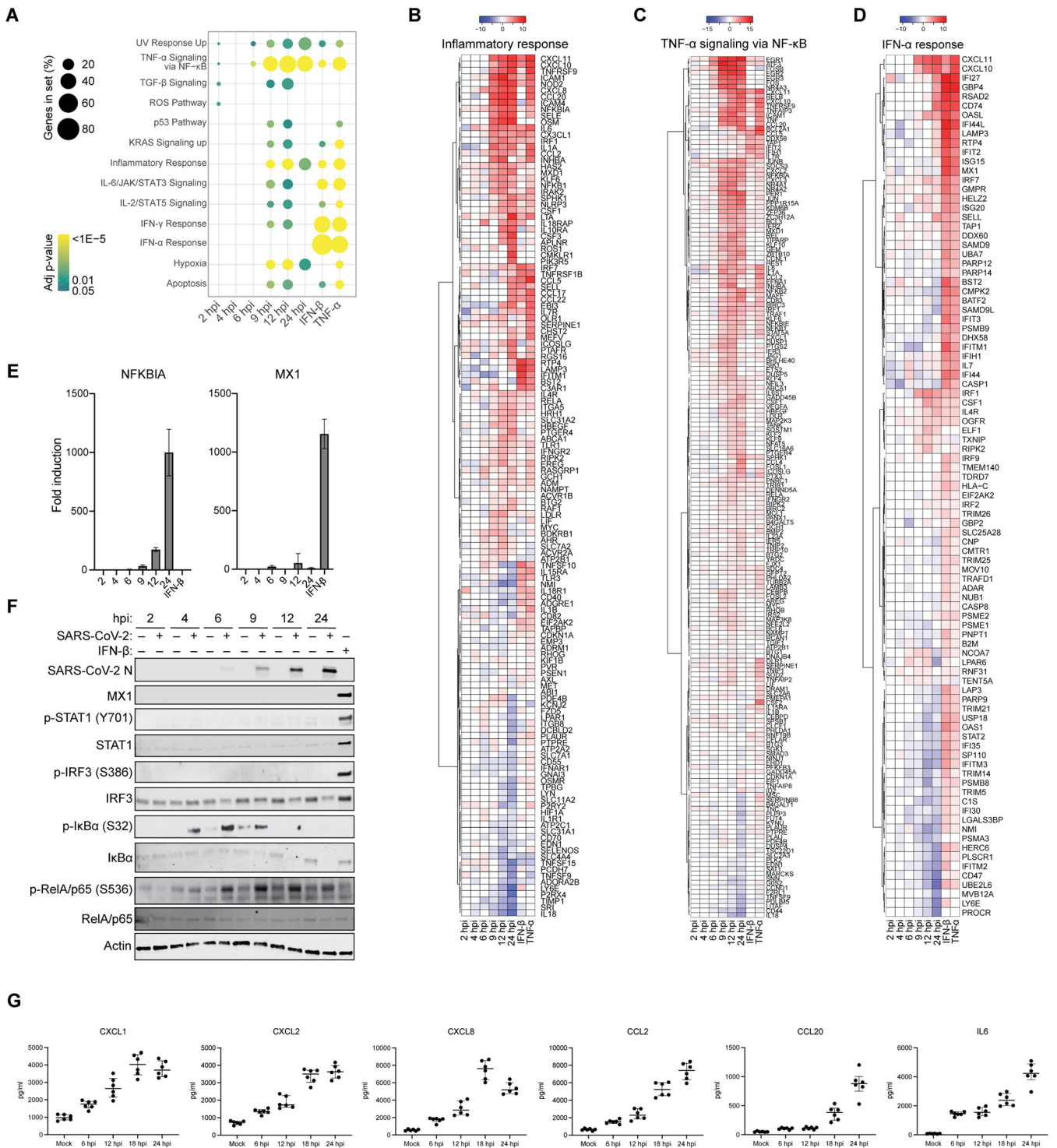


FIG 2 (A) Dot plot visualization of enriched GO terms after RNA-seq analysis of A549-ACE2 cells infected with SARS-CoV-2 (MOI, 2) or treated for 12 h with 100 U/ml IFN-β or 100 ng/ml TNF-α. Gene set enrichment analysis (GSEA) was performed against the GO data sets for biological processes. The color of the dots represents the false discovery rate (FDR) value for each enriched GO term. The size of the dots represents the enrichment signal strength as a percentage of genes included in the complete gene set. (B) Heat map analysis of the \log_2 (fold change) expression levels of differentially expressed genes involved in the inflammatory response after RNA-seq of SARS-CoV-2 infected (MOI, 2) to uninfected A549-ACE2 cells. (C) Heat map analysis of the \log_2 (fold change) expression levels of differentially expressed genes involved in TNF-α signaling via NF-κB after RNA-seq of SARS-CoV-2 infected (MOI, 2) to uninfected A549-ACE2 cells. (D) Heat map analysis of the \log_2 (fold change) expression levels of differentially expressed genes involved in the IFN-α response after RNA-seq of SARS-CoV-2 infected (MOI, 2) to uninfected A549-ACE2 cells. (E) qRT-PCR analysis of A549-ACE2 cells infected with SARS-CoV-2 (MOI, 2). The graph depicts the relative mean accumulation of NFKBIA and MX1 mRNA normalized to human β-actin mRNA levels (n = 3). (F) Western blot analysis for SARS-CoV-2 nucleocapsid (N), Mx1, IRF3, p-IRF3, STAT1, p-STAT1, IκBα, p-IκBα, RelA/p65, p-RelA/p65, and actin of whole-cell lysates from A549-ACE2 cells infected with SARS-CoV-2 (MOI, 2). (G) Multiplexed ELISA analysis on cell culture supernatants from infected A549-ACE2 cells (MOI, 0.5) for the indicated amounts of time for CXCL1, CXCL2, CXCL8, CCL2, CCL20, and IL-6.

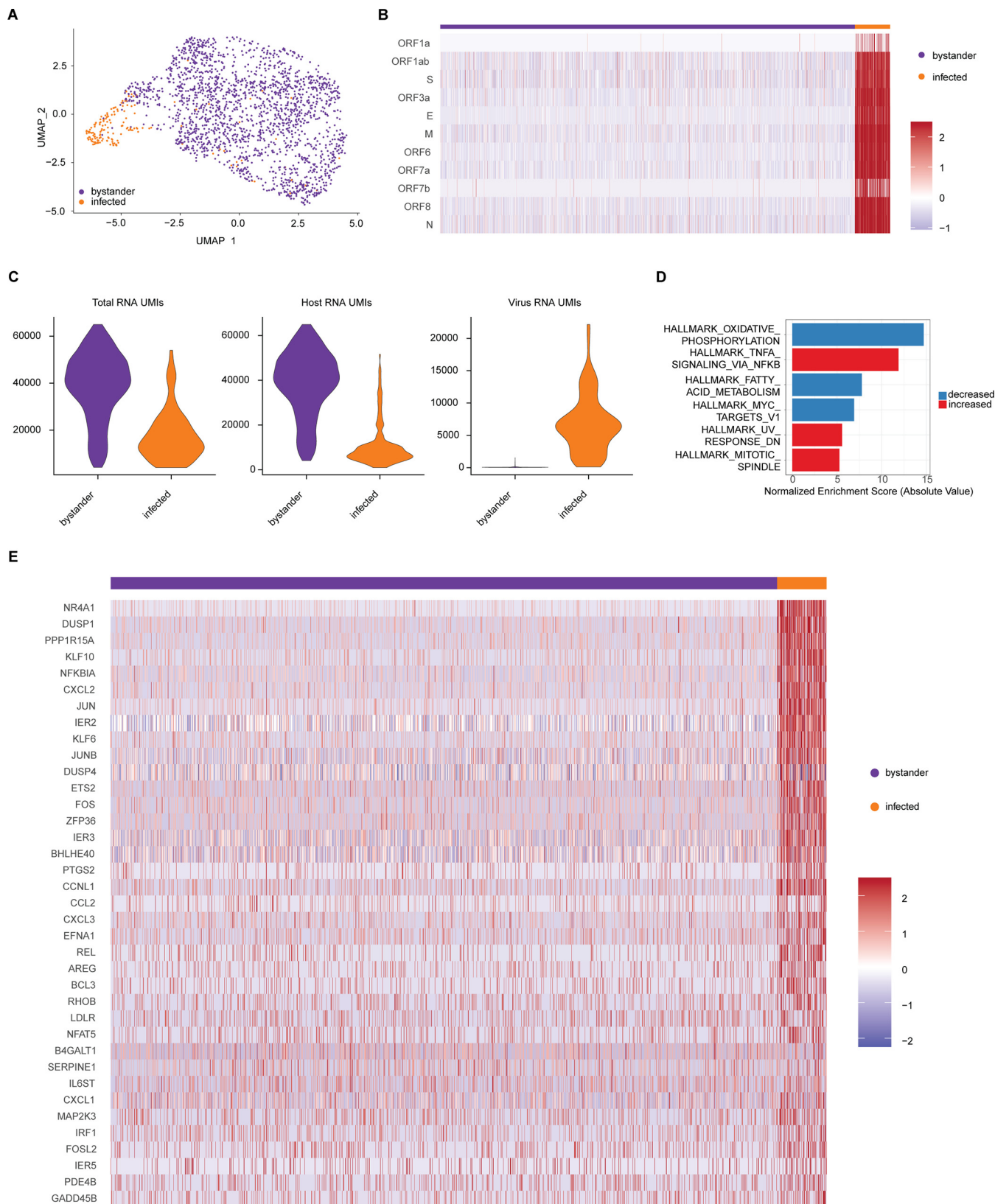


FIG 3 (A) UMAP of single-cell RNA-seq of A549-ACE2 cells infected with SARS-CoV-2 (MOI, 0.01, 24 hpi) showing infected and bystander cells. (B) Single-cell resolution heatmap of SARS-CoV-2 ORFs in infected and bystander cells from single-cell RNA-seq of SARS-CoV-2-infected A549-ACE2 cells (MOI, 0.01, 24 hpi). (C) Violin plots of total RNA UMIs, host RNA UMIs, and virus RNA UMIs for both bystander cells and infected cells from single-cell RNA-seq. (D) Gene set enrichment testing of infected versus bystander cells in scRNA-seq data set (FDR < 0.001). (E) Single-cell resolution heatmap of the genes in hallmark TNF- α signaling via NF- κ B gene set for infected and bystander cells from downsampled data.

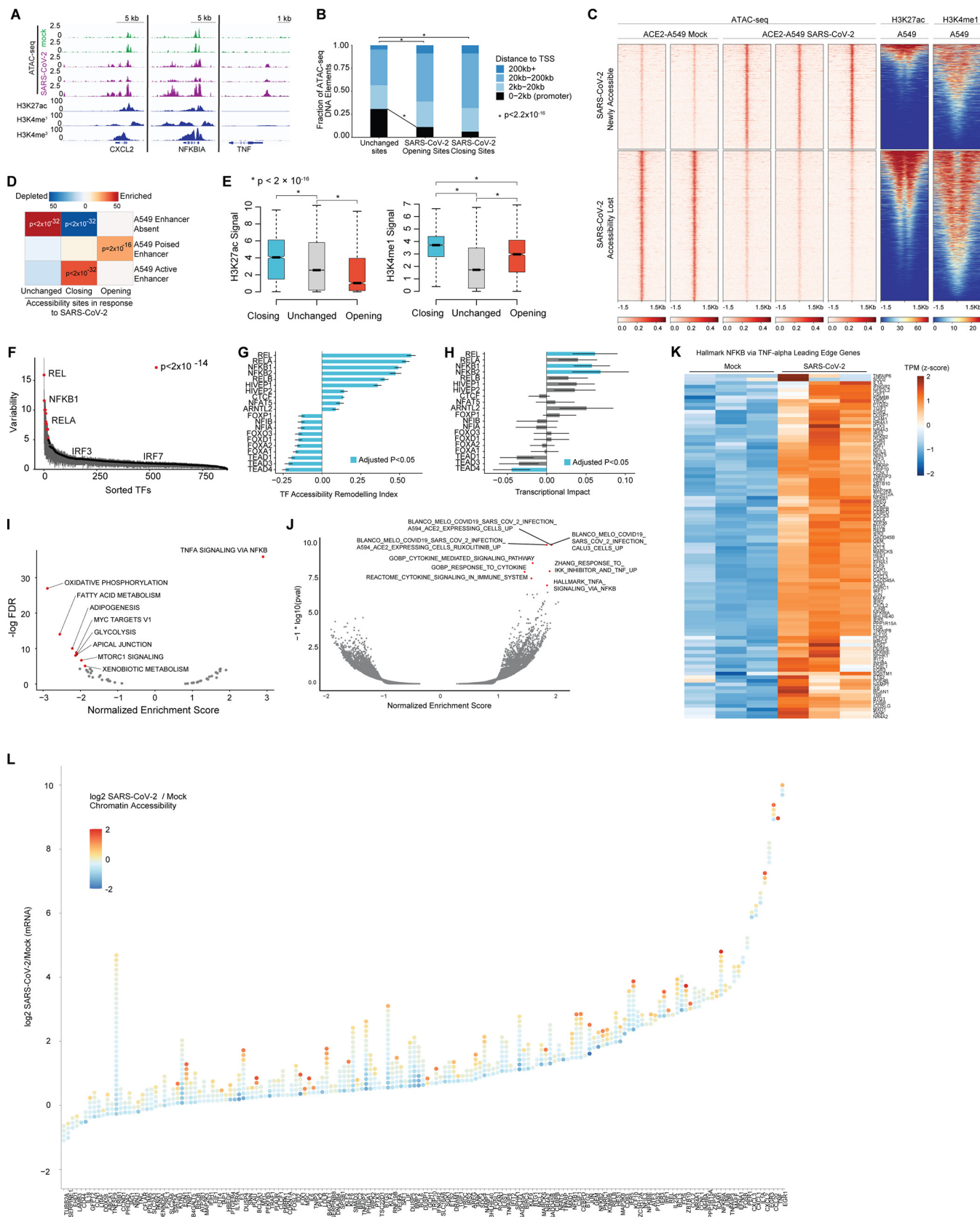


FIG 4 (A) Genome browser view of chromatin accessibility at the indicated loci (*CXCL2*, *NFKB1A*, *TNF*) in mock- or SARS-CoV-2-infected (MOI, 0.1, 24 hpi) ACE2-A549 cells. Also shown are ENCODE tracks for ChIP-seq data of H3K4me1, H3K4me3, and H3K27ac in A549 cells. (B) Fraction of ATAC-seq peaks either (Continued on next page)

that loss of NF- κ B signaling was the molecular basis for decreased viral replication, we transiently expressed a chimeric transcription factor comprised of the DNA-binding domain of RelA fused to the transcriptional activator VPR (VP64-p65-Rta tripartite activator) (29) to agnostically induce gene activation based on enhancer availability, as previously described in wild-type or RelA knockout epithelial cells constitutively overexpressing ACE2 (Fig. 5C). As a control for RelA activation, we also expressed a chimeric transcription factor comprised of the DNA-binding domain of IRF3 (IRF3-VPR) or green fluorescent protein (GFP-VPR) fused to VPR (Fig. 5C). SARS-CoV-2 infection in RelA knockout compared to wild-type cells showed a dramatic loss in viral protein production that could be rescued following reconstitution of RelA/p65 activity (Fig. 5C). In contrast, constitutive IRF3 signaling, which leads to engagement of the IFN-I response, as denoted by IFIT1 expression, inhibited viral replication, which is in accordance with the known IFN sensitivity of SARS-CoV-2 (Fig. 5C) (30, 31). Together, these data suggest that SARS-CoV-2 replication requires the transcriptional output of the NF- κ B signaling pathway.

Given the dominant NF- κ B transcriptional signature generated during SARS-CoV-2 infection alongside its apparent necessity for viral replication, we next sought to determine whether NF- κ B constitutes a viable therapeutic target by targeting it with different small-molecule inhibitors known to affect NF- κ B signaling. To that end, we treated A549-ACE2 cells with BAY11-7082 (an inhibitor of I κ B α phosphorylation), MG115 (a proteasome inhibitor preventing proteolytic degradation of I κ B α), parthenolide (an inhibitor of I κ B α phosphorylation), or p-xyleneselenocyanate (an inhibitor of p50 DNA-binding activity) prior to infection with SARS-CoV-2, and both cell viability and efficacy in inhibiting viral replication were measured 24 hpi (Fig. 5D). For each compound, inhibition of NF- κ B resulted in a modest to significant reduction of infected cells, with no or minimal cytotoxic effects at low drug concentrations. To further validate these findings, we analyzed cells treated with BAY11-7082 or MG115 prior to infection with SARS-CoV-2 by Western blotting (Fig. 5E) or qRT-PCR (Fig. 5F) and observed a significant inhibition in BAY11-7082-treated cells and a near complete loss of viral protein and RNA expression in response to MG115. Consistent with these data, RNA-seq analysis of SARS-CoV-2-infected A549-ACE2 cells treated with BAY11-7082 or MG115 compared to dimethyl sulfoxide (DMSO) treatment demonstrates efficient inhibition of viral reads detected (Fig. 5G) as well as NF- κ B-related genes, such as *CXCL2*, *NFKBIA*, *JUN*, and *JUNB* (Fig. 5H). In addition, we observed a significant reduction of secreted proinflammatory cytokines and chemokines in response to SARS-CoV-2 infection in A549-ACE2 cells after BAY11-7082 compared to DMSO treatment (Fig. 5I).

DISCUSSION

The SARS-CoV-2 pandemic has imposed a significant burden on global health. In an effort to better understand the underlying biology of COVID-19 and identify potential

FIG 4 Legend (Continued)

unchanged, gaining accessibility (SARS-CoV-2 opening sites), or losing accessibility (SARS-CoV-2 closing sites) in A549-ACE2 cells infected with SARS-CoV-2 (MOI, 0.1, 24 hpi) compared to uninfected cells, stratified by distance to transcriptional start sites (TSS). (C) Signals for open chromatin (ATAC-seq), H3K4me1, and H3K27ac at all dynamic accessible sites in response to SARS-CoV-2 infection. ATAC-seq color scale shows the number of ATAC-seq fragments per base pair, normalized to number of fragments in ATAC-seq DNA elements. The color scale for H3K27ac and H3K4me1 ChIP-seq shows the fold enrichment/input per bp. Heatmaps show the mean value per 5-bp bin. (D) Heatmap indicating enrichment and depletion of indicated enhancer types (absent, H3K4me1⁻ H3K27ac⁻; poised, H3K4me1⁺ H3K27ac⁻; active, H3K4me1⁺ H3K27ac⁺) in unchanged, opening, and closing accessibility sites after ATAC-Seq in A549-ACE2 cells infected with SARS-CoV-2 (MOI, 0.1, 24 hpi). (E) Boxplot of H3K27ac (left) and H3K4me1 (right) signal in unchanged, opening, and closing accessibility sites in response to SARS-CoV-2 infection. *P* values were calculated using a Mann-Whitney U-test and adjusted for multiple comparisons by the Holm-Bonferroni method. (F) Ranked plot of variability in chromatin accessibility by transcription factor motif in A549-ACE2 cells infected with SARS-CoV-2 (MOI, 0.1, 24 hpi) as measured by chromVAR. (G) Bar chart of the top and bottom 10 transcription factor motifs in transcriptional impact. (H) Volcano plot of gene set enrichment analysis of differentially expressed genes in A549-ACE2 cells infected with SARS-CoV-2 (MOI, 0.1, 24 hpi). (I) Volcano plot of gene set enrichment analysis of genes associated with differentially accessible chromatin in A549-ACE2 cells infected with SARS-CoV-2 (MOI, 0.1, 24 hpi). (K) Heatmap indicating row-normalized transcripts per million (TPM) from RNA-sequencing of SARS-CoV-2 infected (MOI, 0.1, 24 hpi) and mock-infected ACE2-A549 cells. Three biological replicates per condition are shown. (L) Gain and losses of regulatory elements for the top 50 most differentially expressed genes associated with SARS-CoV-2 infection. Top 25 genes associated with SARS-CoV-2 infection with highest and lowest log₂(fold change) gene expression changes are shown. Each gene is illustrated by a stack of diamonds, where each diamond represents a chromatin peak associated with the gene. Red diamonds denote peaks gained in infection, and blue diamonds denote peaks that were lost.

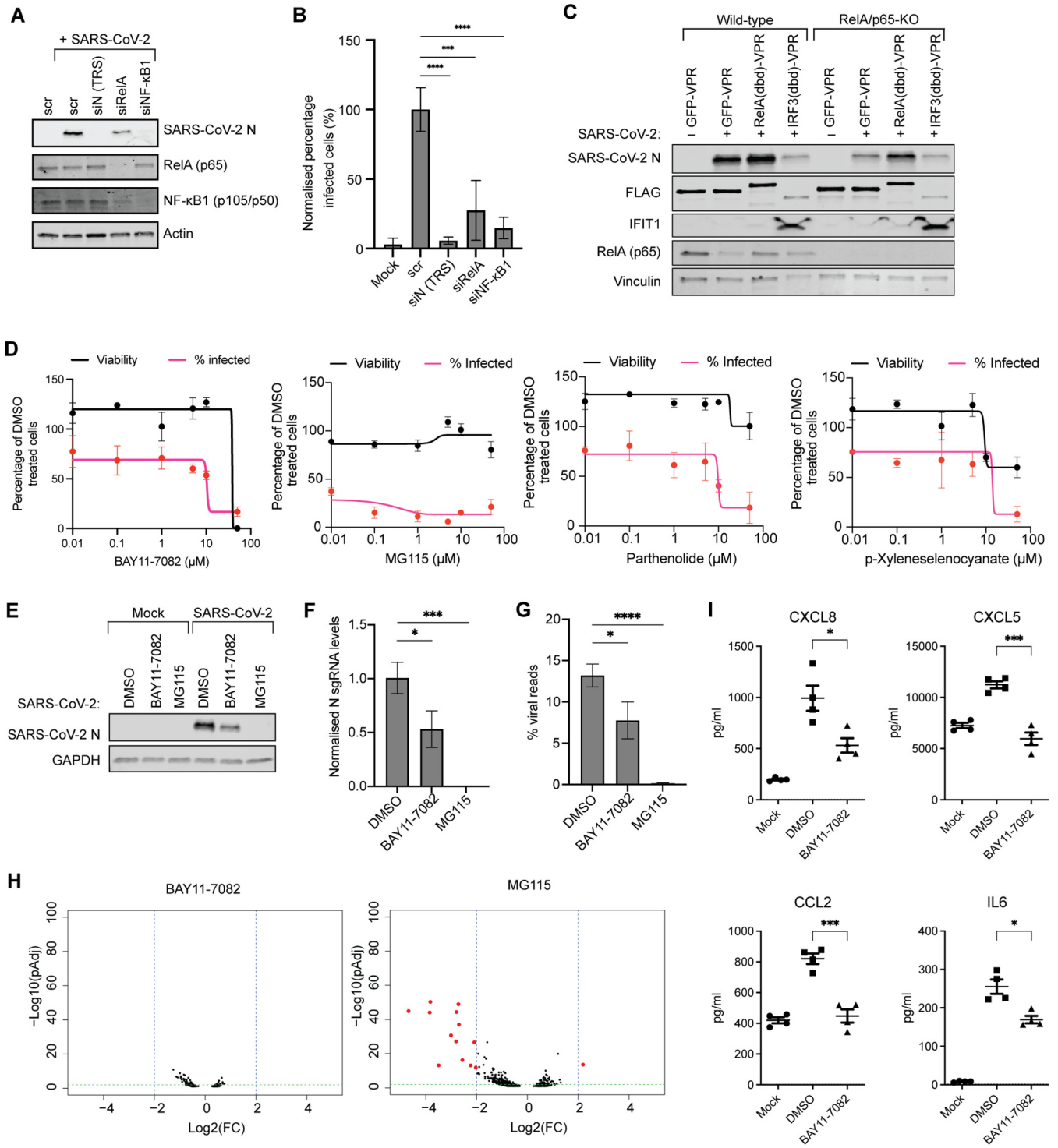


FIG 5 (A) Western blot analysis of whole-cell lysates of siRNA-treated A549-ACE2 cells infected with SARS-CoV-2 (MOI, 0.1, 24 hpi). (B) Quantitation of siRNA-treated A549-ACE2 cells infected with SARS-CoV-2 (MOI, 0.1, 24 hpi) exhibiting nucleocapsid staining in immunofluorescence microscopy. Bar graphs shows the mean percentage of nucleocapsid-positive cells normalized to cells treated with a nontargeting control siRNA. Error bars indicate the standard deviations from eight independent biological replicates. Statistical significance was determined by an unpaired two-sample two-tailed *t* test (***, *P* < 0.001; ****, *P* < 0.0001). (C) Western blot analysis of whole-cell lysates of HeLa-ACE2 or HeLa-p65-KO-ACE2 cells transiently expressing the transcriptional activator VPR fused to the RelA/p65 or IRF3 DNA-binding domains or a GFP control infected with SARS-CoV-2 (MOI, 0.1, 24 hpi). (D) Dose-response analysis of A549-ACE2 cells treated with BAY11-7082, MG115, parthenolide, or p-xyleneselenocyanate at the indicated concentrations and infected with SARS-CoV-2 (MOI, 0.1, 24 hpi). Viral infection and cell viability were quantified and normalized to DMSO-treated samples from 3 independent biological replicates. Percent infection (magenta) and cytotoxicity (black) are shown. (E) Western blot analysis of A549-ACE2 cells treated with DMSO, 10 μM BAY11-7082, or 1 μM MG115 and infected with SARS-CoV-2 (MOI, 0.1, 24 hpi). (F) qRT-PCR analysis of A549-ACE2 cells treated with DMSO, 10 μM BAY11-7082, or 1 μM MG115 and infected with SARS-CoV-2 (MOI, 0.1, 24 hpi). The graph depicts the relative mean accumulation of SARS-CoV-2 nucleocapsid subgenomic RNA (sgN) (Continued on next page)

novel therapeutic strategies, we characterized the cellular inflammatory response to SARS-CoV-2 infection in human lung epithelial cells. These efforts identified NF- κ B as a central transcriptional node responsible for much of the inflammation induced by SARS-CoV-2. More specifically, we show that SARS-CoV-2 infection drives NF- κ B signaling at epigenetic, transcriptional, protein, and posttranslational levels, and that NF- κ B is required for viral replication and the resulting cytokine response. The kinetics of NF- κ B activation was found to be dependent on viral load, suggesting that the accumulation of PAMPs, such as viral dsRNA or misfolded proteins, are responsible for inducing a cellular stress response culminating in the degradation of I κ B α and subsequent translocation of the p65:p50 heterodimer to the nucleus (14). The results of our scRNA-seq analysis further corroborated the activation of NF- κ B and demonstrated that this signature is derived directly from infected cells, indicating that the process of virus replication was responsible for IKK activation. These results are in agreement with previously published scRNA-seq data by other groups showing that infected primary human airway cells also demonstrate a strong NF- κ B signature (32, 33). The data are also consistent with the observed stress response seen in scRNA-seq of SARS-CoV-2-infected Vero E6 cells and in scRNA-seq of dissociated tumors unrelated to SARS-CoV-2 work (20, 34). Regardless of what aspect of virus replication is responsible for IKK activation, nuclear translocation of NF- κ B engages cognate enhancers and induces a broad array of target genes that include the proinflammatory cytokines *TNF*, *IL-1*, and *IL-6*, among others (12). Based on the silencing of p65 and p50, we demonstrate that active NF- κ B signaling is critical for effective viral replication *in vitro*. We further corroborate these findings when enabling constant RelA/p65 signaling by expressing a VPR transcriptional activator fused to the RelA DNA-binding domain, which successfully rescued virus replication in cells devoid of NF- κ B biology. While these data do not exclude the possibility of an IKK-mediated mechanism of posttranslational modification of viral proteins, they suggest that SARS-CoV-2 replication requires the upregulation of one or more NF- κ B target genes. While our RNA-seq analysis demonstrates that small-molecule targeting of NF- κ B by BAY11-7082 or MG115 effectively inhibits induction of cytokines and other classical NF- κ B-target genes, it remains difficult to deconvolute the molecular basis for what gene(s) is responsible for this phenotype.

While there are many broadly acting small-molecule inhibitors of the NF- κ B pathway, there are no specific FDA-approved inhibitors of NF- κ B. In this study, we tested several compounds and molecular strategies to target different components of the NF- κ B signaling pathway, ranging from inhibition of IKK activity and subsequent phosphorylation of I κ B α to inhibition of DNA-binding activity of the NF- κ B transcription factor. As a result, we found that SARS-CoV-2 replication can be effectively blocked or reduced by targeting NF- κ B biology. An added theoretical benefit of this strategy is the simultaneous blocking of the release of proinflammatory cytokines, which are also largely regulated by NF- κ B and are a hallmark of COVID-19 pathology. However, the complex nature of NF- κ B, a key regulator of many cellular processes, including cell survival and proliferation, also makes it a difficult pathway to target, which is reflected by the lack of FDA-approved inhibitors of NF- κ B (35).

Due to the central role of NF- κ B in orchestrating the innate and adaptive immune response, it is unsurprising that many virus families have evolved mechanisms of suppressing NF- κ B signaling (36). For example, members of the *Picornaviridae* family, such as coxsackievirus, hepatitis A virus, and foot-and-mouth disease virus, possess 3C and

FIG 5 Legend (Continued)

normalized to human β -actin mRNA levels from three independent biological replicates with error bars representing the standard deviations. Statistical significance was determined by unpaired two-sample two-tailed *t* tests (*, $P < 0.05$; ***, $P < 0.001$). (G) Mean percentage of viral reads over total mapped reads in RNA-seq from SARS-CoV-2-infected A549-ACE2 cells (MOI, 0.1, 24 hpi) treated with 10 μ M BAY11-7082 or 1 μ M MG115 compared to DMSO from three independent biological replicates. Statistical significance was determined by unpaired two-sample two-tailed *t* tests (*, $P < 0.05$; ****, $P < 0.0001$). (H) Volcano plots depicting differentially expressed genes from RNA-seq analysis of SARS-CoV-2 (MOI, 0.1, 24 hpi) infected A549-ACE2 cells treated with DMSO compared to 10 μ M BAY11-7082 or 1 μ M MG115. Red dots indicate genes with a \log_2 (fold change) greater than 2 or less than -2 and an adjusted *P* value of less than 0.05. (I) Multiplexed ELISA analysis for CXCL5, CXCL8, CCL2, and IL-6 on cell culture supernatants from infected A549-ACE2 cells (MOI, 0.5) treated with DMSO or 10 μ M BAY11-7082.

3C-like proteases, which can cleave critical host proteins required for the activation of NF- κ B, including MAVS, TRIF, TAK, and NEMO (37–39). Another example is porcine reproductive and respiratory syndrome virus (PRRSV), a member of the *Coronaviridae* family, whose Papain-like protease prevents polyubiquitination of I κ B α , which is required for NF- κ B activation (40). This strategy is also common among multiple herpesviruses, such as human betaherpesvirus (HCMV), herpes simplex virus 1 (HSV-1), and Kaposi's sarcoma herpesvirus (41–43). Other mechanisms of suppression of NF- κ B activation include inhibition of the phosphorylation of IKK α and IKK β by vaccinia virus, human cytomegalovirus, and influenza A virus (44–49), direct binding of the p50 and p65 subunits by viral proteins to prevent nuclear translocation or activation, such as HSV-1 (50), competitive binding to the nuclear import factors importin- α and importin- β to prevent nuclear translocation of NF- κ B, e.g., Japanese encephalitis virus or Hantaan virus (51, 52), and prevention of the ubiquitination and subsequent degradation of I κ B α by molecular mimicry of an I κ B α motif by poxvirus protein A49 (53).

However, with the exception of oncogenic viruses, it is much rarer that viruses rely on NF- κ B for essential proviral functions. Oncogenic viruses induce persistent activation of NF- κ B, which contributes to the oncogenic transformation of cells, best exemplified by human T-cell leukemia virus type 1 (HTLV-1) and Epstein-Barr virus (EBV) (54). In another example, all enhancer regions of primate lentiviral long terminal repeats, including for HIV-1, contain one or more NF- κ B binding sites, which recruit p50:p65 heterodimers to the integrated provirus and enable transcription of viral genes by the host cell machinery (55). In fact, early during HIV-1 and HIV-2 infections, it has been reported that the immediate-early viral gene product Tat directly induces NF- κ B activation by promoting p65 DNA binding and inhibiting the NF- κ B repressor I κ B α (56). While a critical role of NF- κ B for oncoviral or lentiviral propagation is easily explained, the finding that influenza A virus (IAV) also has been shown to depend on NF- κ B is more surprising. IAV replication was significantly diminished *in vitro* using BAY11-7082, BAY11-7085, and SC75741, drugs targeting NF- κ B activation (57–59), as well as using dominant-negative mutants of IKK β or I κ B α (60). These findings were recapitulated *in vivo* as well using BAY11-7085 in mouse models, although we were unable to recapitulate these data using SARS-CoV-2 in our hamster model (61). Despite all these studies suggesting a role for NF- κ B in IAV replication, the mechanism underlying these observations remains unclear.

We demonstrate that SARS-CoV-2 infection induces a strong and persistent NF- κ B transcriptional response that mediates the induction of proinflammatory cytokines and chemokines as well as one or more NF- κ B-driven genes that are essential for viral replication. These data provide a biological basis for the imbalanced host response observed in SARS-CoV-2-infected cells and COVID-19 patients as driven by dependencies of the virus for efficient replication. While it has been shown that SARS-CoV-2 is susceptible to the actions of type I IFN (62, 63) and therefore has evolved several mechanisms to suppress the IFN-I response (19–24), we have also previously shown (18) that this antagonized IFN-I response corresponds to an exuberant inflammatory host response. Here, we demonstrate that this is orchestrated by the NF- κ B family of transcription factors, despite the negative implications of inducing a strong NF- κ B-mediated innate and adaptive immune response for the virus. These results further explain the pathogenicity of COVID-19, which is characterized by cytokine-driven hyperinflammation of tissues.

MATERIALS AND METHODS

Cell culture. Angiotensin-converting enzyme 2 (ACE2)-expressing human adenocarcinoma alveolar basal epithelial cells (A549-ACE2) have been described previously (26). African green monkey kidney Vero E6 cells (CRL-1586) were purchased from the ATCC. Human adenocarcinoma cervical epithelial HeLa cells (ab255448) and RELA knockout HeLa cells (ab255425) were purchased from Abcam. ACE2-expressing wild-type (HeLa-ACE2) and RELA knockout HeLa (HeLa-p65-KO-ACE2) cells were generated by lentiviral integration as previously described for HEK293T cells (64). A549-ACE2, HeLa-ACE2, and Vero E6 cells were maintained in Dulbecco's modified Eagle medium (DMEM) supplemented with 10% fetal

TABLE 1 Primer sequences used for qPCR

Gene	qPCR primers	
	Forward (5' to 3')	Reverse (5' to 3')
TUBA1A	CGTCACCAACTGGGACGACA	CTTCTCGCGTTGGCCTTGG
ACTB	CGTCACCAACTGGGACGACA	CTTCTCGCGTTGGCCTTGG
NFKBIA	CAATGCTCAGGAGCCCTGTAA	TCTGTTGACATCAGCCCCAC
IFNB1	GTCAGAGTGGAAATCCTAAG	ACAGCATCTGCTGGTTGAAG
MX1	GTGGCTGAGAACAACCTGTG	GGCATCTGGTCACGATCCC
SARS-CoV-2 TRS-N	CTCTTGTAGATCTGTTCTTAAACGAAC	GGTCCACCAAACGTAATGCG
SARS-CoV-2 NSP14	TGGGGYTTTACRGGTAACCT	AACRCGCTTAACAAAGCACTC
SARS-CoV-2 E	ACAGGTACGTTAATAGTTAATAGCGT	ATATTGCAGCAGTACGCACACA

bovine serum (FBS), 100 U/ml penicillin, and 100 μ g/ml streptomycin. All cells were cultured at 37°C and 5% CO₂.

Monoclonal antibody purification. Monoclonal antibody 1C7 was generated using bacterially expressed recombinant SARS-CoV (Urbani strain) nucleocapsid as an immunogen in BALB/c mice. Hybridomas were produced and screened for binding to purified fusion protein by enzyme-linked immunosorbent assay (ELISA). Binding of 1C7 (IgG2a) to the native protein was confirmed by flow cytometry and immunofluorescence on transfected and permeabilized HEK-293T cells, by Western blot analysis using whole-cell lysates from transfected HEK-293T cells and from SARS-CoV-infected cells, and by immunohistochemistry on transfected and infected cells. Cross-reactivity of 1C7 with SARS-CoV-2 nucleocapsid was confirmed by flow cytometry, Western blotting, and immunohistochemistry.

Virus preparation. SARS-related coronavirus 2 (SARS-CoV-2), isolate USA-WA1/2020 (NR-52281), was deposited by the Centers for Disease Control and Prevention and obtained through BEI Resources, NIAID, NIH. SARS-CoV-2 was propagated at a multiplicity of infection (MOI) of 0.001 in Vero E6 cells in DMEM supplemented with 2% FBS and 100 U/ml penicillin and 100 μ g/ml streptomycin. Viral stocks were cleared from cellular debris by centrifugation (4,000 \times *g*, 10 min, 4°C) prior to three buffer exchanges in phosphate-buffered saline (PBS) using Amicon Ultra-15 centrifugal filter units (100-kDa molecular size cutoff). Infectious titers were determined by plaque assay in Vero E6 cells in minimum essential medium supplemented with 2% FBS and 0.7% agarose as described before (18). Virus infections for experiments were performed in DMEM supplemented with 2% FBS and 100 U/ml penicillin and 100 μ g/ml streptomycin for the indicated times and MOIs. For drug treatments, cells were pretreated at the indicated concentrations for 1 h at 37°C prior to SARS-CoV-2 infection. All work involving live SARS-CoV-2 was performed in the CDC/USDA-approved biosafety level 3 (BSL-3) facility of the Icahn School of Medicine at Mount Sinai in accordance with institutional biosafety requirements.

Quantitative real-time PCR. Total RNA was extracted from cells using TRIzol (Invitrogen) and Direct-zol RNA miniprep plus kit (Zymo Research) and treated with DNase I (Zymo Research) according to the manufacturer's instructions. Reverse transcription was performed using SuperScript IV reverse transcriptase (Invitrogen) and oligo(dT) primers. Quantitative real-time PCR was performed using a KAPA SYBR FAST qPCR master mix kit (Kapa Biosystems) on a LightCycler 480 Instrument II (Roche) according to the manufacturer's instructions. Primer sequences used are detailed in Table 1. To quantify viral replication as measured by single guide RNA synthesis, primers specific for the TRS-L and TRS-B (N) sites were used. Delta-delta-cycle threshold ($\Delta\Delta C_T$) values were determined relative to ACTB and normalized to the average from mock-infected samples. Error bars indicate the standard deviations of the means from three biological replicates.

Western blot analysis. Whole-cell lysates were obtained through lysis of cells in radioimmunoprecipitation (RPMI) lysis buffer containing 1% SDS prior to safe removal from the BSL-3 facility. Lysates were analyzed by SDS-PAGE and transferred onto nitrocellulose membranes. Proteins were detected using monoclonal anti-SARS-CoV-2 nucleocapsid (1C7), monoclonal anti-SARS-CoV-2 spike (2B3E5), monoclonal anti-FLAG (M2) (F1804; Sigma-Aldrich), monoclonal anti-actin (ACTN05) (MS-2295; Thermo Scientific), monoclonal anti-glyceraldehyde-3-phosphate dehydrogenase (GAPDH) (14C10) (2118; Cell Signaling), monoclonal anti-vinculin (EPR8185) (ab129002; Abcam), monoclonal anti-ACE2 [EPR4435(2)] (ab239924; Abcam), monoclonal anti- κ B α (E130) (ab32518; Abcam), polyclonal anti-RelA/p65 (ab16502; Abcam), monoclonal anti-p105/p50 (E381) (ab32360; Abcam), monoclonal anti-IRF3 (EPR2418Y) (ab68481; Abcam), monoclonal anti-STAT1 (EPYR2154) (ab92506; Abcam), monoclonal anti-Mx1 (EPR19967) (ab207414; Abcam), monoclonal anti-IFIT1 (D2X9Z) (14769; Cell Signaling), monoclonal anti- κ B α (phospho Ser32) (EPR3148) (ac92700; Abcam), monoclonal anti-RelA/p65 (phospho Ser536) (EP2294Y) (ab76302; Abcam), monoclonal anti-IRF3 (phospho Ser386) (EPR2346) (ab76493; Abcam), and monoclonal anti-STAT1 (phospho Tyr701) (58D6) (9167; Cell Signaling). Primary antibodies were detected using fluorophore-conjugated secondary goat anti-mouse (IRDye 680RD, 926-68070; IRDye 800CW, 926-32210) and goat anti-rabbit (IRDye 680RD, 926-68071; IRDye 800CW, 926-32211) IgG antibodies or horseradish peroxidase-conjugated donkey anti-rabbit IgG (NA934V; Cytiva). Fluorescent signals were detected using a LI-COR Odyssey CLx imaging system and analyzed by Image Studio software (LI-COR). Chemiluminescence was detected using SuperSignal West Femto maximum sensitivity substrate.

Immunofluorescence staining. Cells were fixed in 4% paraformaldehyde for 24 h prior to safe removal from the BSL-3 facility. Fixed cells were permeabilized in 0.2% Triton X-100 in PBS for 15 min at room temperature. After three washes in PBS, cells were blocked for 1 h at room temperature with 3% bovine serum albumin (BSA) in PBS. Cells were immunostained for dsRNA using a mouse monoclonal anti-dsRNA antibody/clone rJ2 (MABE1134; Sigma-Aldrich) overnight at 4°C. After three washes in PBS, primary antibodies were stained for with an Alexa Fluor 488-conjugated goat polyclonal anti-mouse IgG antibody (A-11029; Invitrogen) for 1 h at room temperature. After three washes in PBS, cells were stained for SARS-CoV-2 nucleocapsid with a directly conjugated Alexa Fluor 594 anti-SARS-N antibody (1C7) and for nuclear DNA using 4',6-diamidino-2-phenylindole (DAPI) for 1 h at room temperature. After three washes in PBS, cells were imaged by fluorescence microscopy using an EVOS M5000 imaging system (Invitrogen).

RNA-seq. Total RNA from infected and mock-infected cells was lysed in TRIzol (Invitrogen) and extracted and DNase I treated using a Direct-zol RNA miniprep kit (Zymo Research) according to the manufacturer's instructions. RNA-seq libraries of polyadenylated RNA were prepared using the TruSeq stranded mRNA library prep kit (Illumina) according to the manufacturer's instructions and sequenced on an Illumina NextSeq 500 platform. Raw reads were aligned to the human genome (hg19) using the RNA-Seq Alignment App on BaseSpace (Illumina, CA), following differential expression analysis using DESeq2 (65). To diminish the noise introduced by different culture times, our differential expression analyses were always performed by matching each experimental condition with a corresponding mock-treated sample that was collected at the same time. Differentially expressed genes (DEGs) were characterized for each sample ($|L2FC| > 1$, adjusted P value of < 0.05) and were used as the query to search for enriched biological processes (gene ontology BP) and network analysis of protein interactions using STRING (65). Heatmaps of gene expression levels were constructed using heatmap.2 from the gplot package in R (<https://cran.r-project.org/web/packages/gplots/index.html>). Volcano plots and dot plots were constructed using ggplot2 and custom scripts in R (66). Heatmaps in Fig. 1 were constructed on DEGs belonging to the following Hallmark gene set annotations: M5890, M5911, and M5932 (67). Alignments to the SARS-CoV-2 genome (GenBank accession no. [NC_045512.2](https://www.ncbi.nlm.nih.gov/nuccore/NC_045512.2)) was performed using bowtie2 (68). All non-RNA-seq statistical analyses were performed as indicated in figure legends using prism 8 (GraphPad Software, San Diego, California USA; <https://www.graphpad.com/>).

Multiplexed cytokine ELISA. Cytokine levels in the cell culture supernatant were evaluated using multiplexed ELISA for the following cytokines: CCL2/MCP-1, CCL20/MIP3a, CXCL1/GROa, CXCL2/GROb, CXCL5/ENA-78, CXCL8/IL-8, and IL-6. All antibodies and cytokine standards were purchased as antibody pairs from R&D Systems (Minneapolis, MN) or Peprotech (Rocky Hill, NJ). Individual magnetic Luminex bead sets (Luminex Corp., CA) were coupled to cytokine-specific capture antibodies according to the manufacturer's recommendations. Samples were analyzed on a Luminex MAGPIX platform and quantified using a standard curve. For each bead region, > 50 beads were collected per analyte. The median fluorescence intensity of these beads was recorded for each bead and was used for analysis using a custom R script and a 5P regression algorithm.

ATAC-seq. For ATAC-seq analysis, A549-ACE2 cells were infected at an MOI of 0.1 for 24 h. Upon harvest, cells were trypsinized and collected as a single-cell suspension in complete DMEM. A total of 50,000 cells were isolated and washed twice with ice-cold PBS. Nuclei from washed cell pellets were extracted using lysis buffer (10 mM Tris-HCl, 10 mM NaCl, 3 mM MgCl₂, 0.1% IGEPAL CA-630). Transposition was performed at 37°C for 30 min using the Nextera DNA library prep kit (Illumina), and transposed DNA was purified using the Qiagen MinElute PCR purification kit according to the manufacturer's instructions. At this stage, purified DNA from samples was removed from the BSL-3 facility in accordance with institutional biosafety protocols. DNA was amplified for 12 cycles using barcoded primers (Table 2). Libraries were purified and library assessment was performed using a spectrophotometer (NanoDrop) and automated capillary electrophoresis (Agilent Bioanalyzer). Barcoded libraries were pooled (2 to 4 samples/lane) and run on an Illumina NextSeq 2000 sequencer using 50-bp paired-end reads. For data analysis, quality and adapter filtering was applied to raw reads using trim_galore before aligning to human assembly hg38 with bowtie2 using the default parameters. The Picard tool MarkDuplicates (<http://broadinstitute.github.io/picard/>) was used to remove reads with the same start site and orientation. The BEDTools suite (<http://bedtools.readthedocs.io>) was used to create read density profiles. Enriched regions were discovered using MACS2 and scored against matched input libraries (fold change of > 2 and false discovery rate [FDR]-adjusted P value of < 0.1). A consensus peak atlas was then created by filtering out blacklisted regions (<http://mitra.stanford.edu/kundaje/akundaje/release/blacklists/hg38-human/>) and then merging all peaks within 500 bp. A raw count matrix was computed over this atlas using featureCounts (<http://subread.sourceforge.net/>) with the -p option for fragment counting. The count matrix and all genome browser tracks were normalized to a sequencing depth of 10 million mapped fragments. DESeq2 was used to classify differential peaks between two conditions using a fold change of > 2 and FDR-adjusted P value of < 0.1 . Peak gene associations were made using linear genomic distance to the nearest transcription start site with Homer (<http://homer.ucsd.edu>).

scRNA-seq of viral infections. A549-ACE2 cells were infected at an MOI of 0.01 with SARS-CoV-2 for 24 h in DMEM supplemented with 2% fetal bovine serum (FBS), 100 U/ml penicillin, and 100 μ g/ml streptomycin. After 24 h, infected cells were trypsinized with 0.25% trypsin and collected as a single-cell suspension. Cells were then washed twice with ice-cold $1 \times$ PBS and filtered using a 40- μ m Flowmi cell strainer (Bel-Art Scienceware). Cell count and viability were determined using trypan blue stain and a Countess II automatic cell counter (ThermoFisher Scientific). Based on this cell count, a target cell input volume of 3,000 cells was loaded into a Chromium Controller using Chromium Next Gem (gel bead-in emulsion) single-cell 5' library & gel bead kit v1.1 (10X Genomics) according to the manufacturer's

TABLE 2 Primer sequences used for ATAC-seq sample barcoding

Sample	Primer sequence ^a
Ad1_noMX	AATGATACGGCGACCACCGAGATCTACACTCGTCGGCAGCGTCAGATGTG
Ad2.1_TAAGGCGA	CAAGCAGAAGACGGCATAACGAGATTCGCCTTAGTCTCGTGGGCTCGGAGATGT
Ad2.2_CGTAAGTAG	CAAGCAGAAGACGGCATAACGAGATCTAGTACGGTCTCGTGGGCTCGGAGATGT
Ad2.3_AGGCAGAA	CAAGCAGAAGACGGCATAACGAGATTTCTGCTGTCTCGTGGGCTCGGAGATGT
Ad2.4_TCCTGAGC	CAAGCAGAAGACGGCATAACGAGATGCTCAGGAGTCTCGTGGGCTCGGAGATGT
Ad2.5_GGACTCTG	CAAGCAGAAGACGGCATAACGAGATAGGAGTCCGTCTCGTGGGCTCGGAGATGT
Ad2.6_TAGGCATG	CAAGCAGAAGACGGCATAACGAGATCATGCCTAGTCTCGTGGGCTCGGAGATGT
Ad2.7_CTCTCTAC	CAAGCAGAAGACGGCATAACGAGATGTAGAGAGGTCTCGTGGGCTCGGAGATGT
Ad2.8_CAGAGAGG	CAAGCAGAAGACGGCATAACGAGATCTCTCTGCTCGTGGGCTCGGAGATGT
Ad2.9_GCTACGCT	CAAGCAGAAGACGGCATAACGAGATAGCGTAGCGTCTCGTGGGCTCGGAGATGT
Ad2.10_CGAGGCTG	CAAGCAGAAGACGGCATAACGAGATCAGCCTCGGTCTCGTGGGCTCGGAGATGT
Ad2.11_AAGAGGCA	CAAGCAGAAGACGGCATAACGAGATTCCTCTTGTCTCGTGGGCTCGGAGATGT
Ad2.12_GTAGAGGA	CAAGCAGAAGACGGCATAACGAGATTCCTCTACGTCTCGTGGGCTCGGAGATGT
Ad2.13_GTCGTGAT	CAAGCAGAAGACGGCATAACGAGATATCACGACGTCTCGTGGGCTCGGAGATGT
Ad2.14_ACCACTGT	CAAGCAGAAGACGGCATAACGAGATACAGTGGTGTCTCGTGGGCTCGGAGATGT
Ad2.15_TGGATCTG	CAAGCAGAAGACGGCATAACGAGATCAGATCCAGTCTCGTGGGCTCGGAGATGT
Ad2.16_CCGTTTGT	CAAGCAGAAGACGGCATAACGAGATACAAACGGTCTCGTGGGCTCGGAGATGT
Ad2.17_TGCTGGGT	CAAGCAGAAGACGGCATAACGAGATACCCAGCAGTCTCGTGGGCTCGGAGATGT
Ad2.18_GAGGGGTT	CAAGCAGAAGACGGCATAACGAGATAACCCCTCGTCTCGTGGGCTCGGAGATGT
Ad2.19_AGGTTGGG	CAAGCAGAAGACGGCATAACGAGATCCCAACCTGTCTCGTGGGCTCGGAGATGT
Ad2.20_GTGTGGTG	CAAGCAGAAGACGGCATAACGAGATCACACACGTCTCGTGGGCTCGGAGATGT
Ad2.21_TGGGTTTC	CAAGCAGAAGACGGCATAACGAGATGAAACCCAGTCTCGTGGGCTCGGAGATGT
Ad2.22_TGGTCACA	CAAGCAGAAGACGGCATAACGAGATTGTACCAGTCTCGTGGGCTCGGAGATGT
Ad2.23_TTGACCCT	CAAGCAGAAGACGGCATAACGAGATAGGGTCAAGTCTCGTGGGCTCGGAGATGT
Ad2.24_CCACTCT	CAAGCAGAAGACGGCATAACGAGATAGGAGTGGGTCTCGTGGGCTCGGAGATGT

^aSequences are from Buenrostro et al. (69).

instructions. After GEMs were generated, library preparation of all samples was performed using the Chromium single-cell 5' library kit v1.1 (10X Genomics) according to the manufacturer's instructions. The library was then sequenced on an Illumina NextSeq 500.

scRNA-seq analysis. Sequencing data were processed with Cell Ranger v4.0.0 (10X Genomics, Inc.). Reads were mapped to a combined human (GRCh38) and SARS-CoV-2 (WuhCor1, [NC_045512.2](#), modified to reflect the USA-WA1/2020 strain, MT246667.1) genome reference using Cell Ranger count. Raw gene \times cell counts matrices were analyzed using Seurat (v4.0.1). After an initial filter to remove cells with fewer than 4,000 UMIs (empty droplets) or greater than 65,000 UMIs (doublets) and percent mitochondrial gene expression less than 5% or greater than 40%, count data were subject to natural logarithm normalization, cell cycle scoring, highly variable gene selection, gene expression scaling, and dimensional reduction by principal-component analysis using the developer's defaults. UMIs, mitochondrial gene expression percentage, S cell cycle phase score, and G₂M cell cycle phase score were regressed during gene expression scaling. Further processing included unsupervised clustering analysis using the FindClusters function (resolution, 0.4) and visualization with Uniform Manifold Approximation and Projection (developer's defaults). All gene expression violin plots were plotted using natural logarithm normalized counts and heatmaps with z-scaled counts. Cells were classified as infected or uninfected by performing hierarchical clustering using Ward's minimum variance method on a distance matrix of z-scaled, log-normalized viral gene expression per cell with *k* set to 2. Comparing total viral UMIs per cluster separated cells into high and low viral gene expressing cells, and the cluster with higher viral gene expression was classified as infected.

Differential gene expression (DGE) analyses were conducted using edgeR v3.30.3 (70), with additional modifications for scRNA-seq data (71). Gene \times cell count matrices were extracted from Seurat objects with infection information as metadata. SARS-CoV-2 viral genes were excluded from all differential gene expression analyses and cell cycle scores were calculated using Seurat's CellCycleScoring function. For all analyses, genes expressed (i.e., greater than or equal to 1 UMI) in less than 10% of cells for at least one group were excluded from differential gene expression testing. To identify the transcriptional signature in infected cells, differential expression analysis was conducted by comparing bystander cells to infected cells. To mitigate the dramatic differences in host gene expression between infected cells and bystander cells, transcript counts from infected and bystander cells were randomly downsampled to the median transcript counts/cell of the infected cell group. All cells with counts below this value were excluded from differential expression analyses. edgeR linear models included factors for cell cycle score (S phase and G₂M phase scores), cellular gene detection rate, and infection status. The resulting significantly differentially expressed genes were defined by an adjusted *P* value of <0.0001 and an absolute log₂ fold change of ± 1 . Gene set enrichment testing was conducted using the HALLMARK gene sets from the Molecular Signatures database (MSigDB) with the CAMERA function (72). The parameter use.ranks was set to TRUE to minimize assumptions about data structure of scRNA-seq data compared to bulk RNA-seq or microarray data. Gene set enrichment contrasts were set to compare infected cells versus bystander cells, and significantly enriched gene sets were identified using an adjusted *P* value of less than 0.001.

siRNA-mediated silencing of NF- κ B. RelA/p65 or NF- κ B1 components of NF- κ B were silenced in A549-ACE2 cells by siRNA-mediated RNAi. A549-ACE2 cells were transfected with 36 nM siRNA pools targeting RelA/p65 (L-003533-00-0005; Horizon Discovery), p105/p50 (L-003520-00-0005; Horizon Discovery), or a nontargeting control pool (D-001810-10-20; Horizon Discovery) using RNAiMax according to the manufacturer's instructions. At 48 h posttransfection, cells were retransfected with 36 nM siRNA pools as before. At 24 h posttransfection, cells were infected with SARS-CoV-2 at an MOI of 0.1 for 24 h in DMEM supplemented with 2% FBS. At the time of sample collection, cells were either lysed in RIPA buffer supplemented with 1% SDS and analyzed by Western blotting or fixed in 4% paraformaldehyde and immunostained.

Quantitative immunofluorescence staining. Cells were fixed in 4% paraformaldehyde for 24 h prior to safe removal from the BSL-3 facility. Fixed cells were permeabilized in 0.2% Triton X-100 in PBS for 15 min at room temperature. After three washes in PBS, cells were blocked for 1 h at room temperature with 3% BSA in PBS. Cells were immunostained for SARS-CoV-2 nucleocapsid using a mouse monoclonal anti-SARS-N antibody (clone 1C7) overnight at room temperature. After three washes in PBS, cells were stained with an Alexa Fluor 488-conjugated goat polyclonal anti-mouse IgG antibody (A-11029; Invitrogen) and DAPI for 1 h at room temperature. After three washes in PBS, cells were imaged and quantified on a Celigo imaging cytometer (Nexcelom Bioscience). Graphs depict the average percentage of infected cells normalized to the control from eight biological replicates. Error bars depict the standard deviations.

Plasmid transfections. Approximately 2.4×10^5 HeLa-ACE2 cells were transiently transfected with 0.5 μ g of pCAGGS-GFP-VPR, pCAGGS-RelA/p65(dbd)-VPR, or pCAGGS-IRF3(dbd)-VPR using Lipofectamine 2000 according to the manufacturer's instructions. Transfected cells were treated with 500 nM ruxolitinib to block an antiviral IFN response caused by plasmid transfection. At 24 h posttransfection, medium was changed on the cells in the absence of ruxolitinib. At 48 h posttransfection, cells were infected with SARS-CoV-2 at an MOI of 0.1 for 24 h in DMEM supplemented with 2% FBS. At the time of sample collection, cells were lysed in RIPA buffer supplemented with 1% SDS and analyzed by western.

Viral growth and cytotoxicity in the presence of NF- κ B inhibitors. Approximately 4×10^4 A549-ACE2 cells were seeded in 96-well plates. The next day, cells were treated with either DMSO or drugs resuspended in DMSO at six different concentrations (0.01, 0.1, 1, 5, 10, and 50 μ M) in eight replicates per condition. To determine cytotoxic effects of drugs, cell viability was measured 24 h posttreatment using the CellTiter-Glo luminescent cell viability assay (Promega). Cell viability was quantified and normalized to the DMSO control. To determine inhibition of viral replication, 1 h posttreatment cells were infected with SARS-CoV-2 at an MOI of 0.1 for 24 h. Cells were subsequently fixed in 4% paraformaldehyde 24 hpi overnight at 4°C and immunostained for viral nucleocapsid and quantified as described above. The percentage of infected cells was calculated and normalized to the DMSO control.

For Western blot analysis and RNA-seq analysis of drug-treated infected cells, cells were pretreated with DMSO or 10 μ M BAY11-7082 or 1 μ M MG115 for 1 h before infection with SARS-CoV-2 (MOI, 0.1) for 24 h. Cells were lysed in RIPA buffer supplemented with 1% SDS or TRIzol and analyzed as described previously.

Data availability. The raw sequencing data sets generated during this study are available on the NCBI Gene Expression Omnibus (GEO) server under accession number [GSE184536](https://www.ncbi.nlm.nih.gov/geo/query/acc.cgi?acc=GSE184536).

ACKNOWLEDGMENTS

We thank the Bill and Melinda Gates Foundation for their financial support for this work. We also thank Oded Danziger for providing clonal A549-ACE2 cells and Julie Eggenberger for cloning of the pCAGGS-GFP-VPR, pCAGGS-RelA/p65(dbd)-VPR, and pCAGGS-IRF3(dbd)-VPR plasmids. This work was supported by National Institutes of Health grant AI151029-01A1 to B.R.R.

S.U., B.N.P., and B.T.O. wrote the paper; B.T.O., B.R.R., R.C., R.S., S.U., and B.N.P. designed experiments; P.C., R.S.P., B.R.R., and D.B.M. analyzed scRNA-seq data; S.U., B.N.P., I.G., and C.H. performed *in vitro* BSL3 experiments; S.U., A.G., Y.B., and V.C. performed ATAC-seq experiments; A.D. and O.E. analyzed ATAC-seq experiments; B.N.P. performed *in vitro* work related to testing NF- κ B inhibitors; M.P. prepared libraries for Illumina sequencing.

O.E. is a scientific advisor and equity holder in Freenome, Owkin, Volastra Therapeutics, and OneThree Biotech. R.E.S. is on the scientific advisory board of Miromatrix Inc. and is a consultant and speaker for Alnylam Inc.

REFERENCES

- tenOever BR. 2016. The evolution of antiviral defense systems. *Cell Host Microbe* 19:142–149. <https://doi.org/10.1016/j.chom.2016.01.006>.
- Lazear HM, Schoggins JW, Diamond MS. 2019. Shared and distinct functions of type I and type III interferons. *Immunity* 50:907–923. <https://doi.org/10.1016/j.immuni.2019.03.025>.
- Iwasaki A, Medzhitov R. 2004. Toll-like receptor control of the adaptive immune responses. *Nat Immunol* 5:987–995. <https://doi.org/10.1038/ni1112>.
- Honda K, Takaoka A, Taniguchi T. 2006. Type I interferon [corrected] gene induction by the interferon regulatory factor family of transcription

- factors. *Immunity* 25:349–360. <https://doi.org/10.1016/j.immuni.2006.08.009>.
5. Schneider WM, Chevillotte MD, Rice CM. 2014. Interferon-stimulated genes: a complex web of host defenses. *Annu Rev Immunol* 32:513–545. <https://doi.org/10.1146/annurev-immunol-032713-120231>.
 6. Sokol CL, Luster AD. 2015. The chemokine system in innate immunity. *Cold Spring Harb Perspect Biol* 7:a016303. <https://doi.org/10.1101/cshperspect.a016303>.
 7. Proudfoot AE. 2002. Chemokine receptors: multifaceted therapeutic targets. *Nat Rev Immunol* 2:106–115. <https://doi.org/10.1038/nri722>.
 8. Panne D, Maniatis T, Harrison SC. 2007. An atomic model of the interferon-beta enhanceosome. *Cell* 129:1111–1123. <https://doi.org/10.1016/j.cell.2007.05.019>.
 9. Sharma S, tenOever BR, Grandvaux N, Zhou GP, Lin R, Hiscott J. 2003. Triggering the interferon antiviral response through an IKK-related pathway. *Science* 300:1148–1151. <https://doi.org/10.1126/science.1081315>.
 10. Agalioti T, Lomvardas S, Parekh B, Yie J, Maniatis T, Thanos D. 2000. Ordered recruitment of chromatin modifying and general transcription factors to the IFN-beta promoter. *Cell* 103:667–678. [https://doi.org/10.1016/S0092-8674\(00\)00169-0](https://doi.org/10.1016/S0092-8674(00)00169-0).
 11. Taniguchi K, Karin M. 2018. NF-kappaB, inflammation, immunity and cancer: coming of age. *Nat Rev Immunol* 18:309–324. <https://doi.org/10.1038/nri.2017.142>.
 12. Bonizzi G, Karin M. 2004. The two NF-kappaB activation pathways and their role in innate and adaptive immunity. *Trends Immunol* 25:280–288. <https://doi.org/10.1016/j.it.2004.03.008>.
 13. Ghosh S, Karin M. 2002. Missing pieces in the NF-kappaB puzzle. *Cell* 109 (Suppl):S81–S96. [https://doi.org/10.1016/S0092-8674\(02\)00703-1](https://doi.org/10.1016/S0092-8674(02)00703-1).
 14. Karin M, Greten FR. 2005. NF-kappaB: linking inflammation and immunity to cancer development and progression. *Nat Rev Immunol* 5:749–759. <https://doi.org/10.1038/nri1703>.
 15. Vallabhapurapu S, Karin M. 2009. Regulation and function of NF-kappaB transcription factors in the immune system. *Annu Rev Immunol* 27: 693–733. <https://doi.org/10.1146/annurev.immunol.021908.132641>.
 16. Wang W, Xu L, Su J, Peppelenbosch MP, Pan Q. 2017. Transcriptional regulation of antiviral interferon-stimulated genes. *Trends Microbiol* 25: 573–584. <https://doi.org/10.1016/j.tim.2017.01.001>.
 17. Garcia-Sastre A. 2017. Ten strategies of interferon evasion by viruses. *Cell Host Microbe* 22:176–184. <https://doi.org/10.1016/j.chom.2017.07.012>.
 18. Blanco-Melo D, Nilsson-Payant BE, Liu WC, Uhl S, Hoagland D, Moller R, Jordan TX, Oishi K, Panis M, Sachs D, Wang TT, Schwartz RE, Lim JK, Albrecht RA, tenOever BR. 2020. Imbalanced host response to SARS-CoV-2 drives development of COVID-19. *Cell* 181:1036–1045. <https://doi.org/10.1016/j.cell.2020.04.026>.
 19. Lowery SA, Sariol A, Perlman S. 2021. Innate immune and inflammatory responses to SARS-CoV-2: implications for COVID-19. *Cell Host Microbe* 29:1052–1062. <https://doi.org/10.1016/j.chom.2021.05.004>.
 20. Miorin L, Kehrer T, Sanchez-Aparicio MT, Zhang K, Cohen P, Patel RS, Cupic A, Makio T, Mei M, Moreno E, Danziger O, White KM, Rathnasinghe R, Uccellini M, Gao S, Aydiillo T, Mena I, Yin X, Martin-Sancho L, Krogan NJ, Chanda SK, Schotsaert M, Wozniak RW, Ren Y, Rosenberg BR, Fontoura BMA, Garcia-Sastre A. 2020. SARS-CoV-2 Orf6 hijacks Nup98 to block STAT nuclear import and antagonize interferon signaling. *Proc Natl Acad Sci U S A* 117:28344–28354. <https://doi.org/10.1073/pnas.2016650117>.
 21. Lei X, Dong X, Ma R, Wang W, Xiao X, Tian Z, Wang C, Wang Y, Li L, Ren L, Guo F, Zhao Z, Zhou Z, Xiang Z, Wang J. 2020. Activation and evasion of type I interferon responses by SARS-CoV-2. *Nat Commun* 11:3810. <https://doi.org/10.1038/s41467-020-17665-9>.
 22. Xia H, Cao Z, Xie X, Zhang X, Chen JY, Wang H, Menachery VD, Rajsbaum R, Shi PY. 2020. Evasion of type I interferon by SARS-CoV-2. *Cell Rep* 33: 108234. <https://doi.org/10.1016/j.celrep.2020.108234>.
 23. Wu J, Shi Y, Pan X, Wu S, Hou R, Zhang Y, Zhong T, Tang H, Du W, Wang L, Wo J, Mu J, Qiu Y, Yang K, Zhang LK, Ye BC, Qi N. 2021. SARS-CoV-2 ORF9b inhibits RIG-I-MAVS antiviral signaling by interrupting K63-linked ubiquitination of NEMO. *Cell Rep* 34:108761. <https://doi.org/10.1016/j.celrep.2021.108761>.
 24. Fu YZ, Wang SY, Zheng ZQ, Yi H, Li WW, Xu ZS, Wang YY. 2021. SARS-CoV-2 membrane glycoprotein M antagonizes the MAVS-mediated innate antiviral response. *Cell Mol Immunol* 18:613–620. <https://doi.org/10.1038/s41423-020-00571-x>.
 25. Hoffmann M, Kleine-Weber H, Schroeder S, Kruger N, Herrler T, Erichsen S, Schiergens TS, Herrler G, Wu NH, Nitsche A, Muller MA, Drosten C, Pohlmann S. 2020. SARS-CoV-2 cell entry depends on ACE2 and TMPRSS2 and is blocked by a clinically proven protease inhibitor. *Cell* 181:271–280. <https://doi.org/10.1016/j.cell.2020.02.052>.
 26. Daniloski Z, Jordan TX, Wessels HH, Hoagland DA, Kasela S, Legut M, Maniatis S, Mimitou EP, Lu L, Geller E, Danziger O, Rosenberg BR, Phatnani H, Smibert P, Lappalainen T, tenOever BR, Sanjana NE. 2021. Identification of required host factors for SARS-CoV-2 infection in human cells. *Cell* 184:92–105. <https://doi.org/10.1016/j.cell.2020.10.030>.
 27. Li Y, Renner DM, Comar CE, Whelan JN, Reyes HM, Cardenas-Diaz FL, Truitt R, Tan LH, Dong B, Alysandratos KD, Huang J, Palmer JN, Adappa ND, Kohanski MA, Kotton DN, Silverman RH, Yang W, Morrissey EE, Cohen NA, Weiss SR. 2021. SARS-CoV-2 induces double-stranded RNA-mediated innate immune responses in respiratory epithelial-derived cells and cardiomyocytes. *Proc Natl Acad Sci U S A* 118:e2022643118. <https://doi.org/10.1073/pnas.2022643118>.
 28. Zhang K, Miorin L, Makio T, Dehghan I, Gao S, Xie Y, Zhong H, Esparza M, Kehrer T, Kumar A, Hobman TC, Ptak C, Gao B, Minna JD, Chen Z, Garcia-Sastre A, Ren Y, Wozniak RW, Fontoura BMA. 2021. Nsp1 protein of SARS-CoV-2 disrupts the mRNA export machinery to inhibit host gene expression. *Sci Adv* 7:abe7386. <https://doi.org/10.1126/sciadv.abe7386>.
 29. Chavez A, Scheiman J, Vora S, Pruitt BW, Tuttle M, P R Iyer E, Lin S, Kiani S, Guzman CD, Wiegand DJ, Ter-Ovanesyan D, Braff JL, Davidsohn N, Housden BE, Perrimon N, Weiss R, Aach J, Collins JJ, Church GM. 2015. Highly efficient Cas9-mediated transcriptional programming. *Nat Methods* 12:326–328. <https://doi.org/10.1038/nmeth.3312>.
 30. Lokugamage KG, Hage A, de Vries M, Valero-Jimenez AM, Schindewolf C, Dittmann M, Rajsbaum R, Menachery VD. 2020. Type I interferon susceptibility distinguishes SARS-CoV-2 from SARS-CoV. *J Virol* 94:e01410-20. <https://doi.org/10.1128/JVI.01410-20>.
 31. Vanderheiden A, Ralfs P, Chirkova T, Upadhyay AA, Zimmerman MG, Bedoya S, Aoued H, Tharp GM, Pellegrini KL, Manfredi C, Sorscher E, Mainou B, Lobby JL, Kohlmeier JE, Lowen AC, Shi PY, Menachery VD, Anderson LJ, Grakoui A, Bosinger SE, Suthar MS. 2020. Type I and type III interferons restrict SARS-CoV-2 infection of human airway epithelial cultures. *J Virol* 94:e00985-20. <https://doi.org/10.1128/JVI.00985-20>.
 32. Ravindra NG, Alfajaro MM, Gasque V, Huston NC, Wan H, Szigeti-Buck K, Yasumoto Y, Greaney AM, Habet V, Chow RD, Chen JS, Wei J, Filler RB, Wang B, Wang G, Niklason LE, Montgomery RR, Eisenbarth SC, Chen S, Williams A, Iwasaki A, Horvath TL, Foxman EF, Pierce RW, Pyle AM, van Dijk D, Wilen CB. 2021. Single-cell longitudinal analysis of SARS-CoV-2 infection in human airway epithelium identifies target cells, alterations in gene expression, and cell state changes. *PLoS Biol* 19:e3001143. <https://doi.org/10.1371/journal.pbio.3001143>.
 33. Fiege JK, Thiede JM, Nanda HA, Matchett WE, Moore PJ, Montanari NR, Thielen BK, Daniel J, Stanley E, Hunter RC, Menachery VD, Shen SS, Bold TD, Langlois RA. 2021. Single cell resolution of SARS-CoV-2 tropism, antiviral responses, and susceptibility to therapies in primary human airway epithelium. *PLoS Pathog* 17:e1009292. <https://doi.org/10.1371/journal.ppat.1009292>.
 34. O'Flanagan CH, Campbell KR, Zhang AW, Kabeer F, Lim JLP, Biele J, Eirew P, Lai D, McPherson A, Kong E, Bates C, Borkowski K, Wiens M, Hewitson B, Hopkins J, Pham J, Ceglia N, Moore R, Mungall AJ, McAlpine JN, Shah SP, Aparicio S, CRUK IMAXT Grand Challenge Team. 2019. Dissociation of solid tumor tissues with cold active protease for single-cell RNA-seq minimizes conserved collagenase-associated stress responses. *Genome Biol* 20:210. <https://doi.org/10.1186/s13059-019-1830-0>.
 35. Oeckinghaus A, Ghosh S. 2009. The NF-kappaB family of transcription factors and its regulation. *Cold Spring Harb Perspect Biol* 1:a000034. <https://doi.org/10.1101/cshperspect.a000034>.
 36. Deng L, Zeng Q, Wang M, Cheng A, Jia R, Chen S, Zhu D, Liu M, Yang Q, Wu Y, Zhao X, Zhang S, Liu Y, Yu Y, Zhang L, Chen X. 2018. Suppression of NF-kappaB activity: a viral immune evasion mechanism. *Viruses* 10:409. <https://doi.org/10.3390/v10080409>.
 37. Rui Y, Su J, Wang H, Chang J, Wang S, Zheng W, Cai Y, Wei W, Gordy JT, Markham R, Kong W, Zhang W, Yu XF. 2017. Disruption of MDA5-mediated innate immune responses by the 3C proteins of coxsackievirus A16, coxsackievirus A6, and enterovirus D68. *J Virol* 91:e00546-17. <https://doi.org/10.1128/JVI.00546-17>.
 38. Wang D, Fang L, Li K, Zhong H, Fan J, Ouyang C, Zhang H, Duan E, Luo R, Zhang Z, Liu X, Chen H, Xiao S. 2012. Foot-and-mouth disease virus 3C protease cleaves NEMO to impair innate immune signaling. *J Virol* 86: 9311–9322. <https://doi.org/10.1128/JVI.00722-12>.
 39. Wang D, Fang L, Wei D, Zhang H, Luo R, Chen H, Li K, Xiao S. 2014. Hepatitis A virus 3C protease cleaves NEMO to impair induction of beta interferon. *J Virol* 88:10252–10258. <https://doi.org/10.1128/JVI.00869-14>.

40. Sun Z, Chen Z, Lawson SR, Fang Y. 2010. The cysteine protease domain of porcine reproductive and respiratory syndrome virus nonstructural protein 2 possesses deubiquitinating and interferon antagonism functions. *J Virol* 84:7832–7846. <https://doi.org/10.1128/JVI.00217-10>.
41. Kwon KM, Oh SE, Kim YE, Han TH, Ahn JH. 2017. Cooperative inhibition of RIP1-mediated NF-kappaB signaling by cytomegalovirus-encoded deubiquitinase and inactive homolog of cellular ribonucleotide reductase large subunit. *PLoS Pathog* 13:e1006423. <https://doi.org/10.1371/journal.ppat.1006423>.
42. Ye R, Su C, Xu H, Zheng C. 2017. Herpes simplex virus 1 ubiquitin-specific protease UL36 abrogates NF-kappaB activation in DNA sensing signal pathway. *J Virol* 91:e02417-16. <https://doi.org/10.1128/JVI.02417-16>.
43. Inn KS, Lee SH, Rathbun JY, Wong LY, Toth Z, Machida K, Ou JH, Jung JU. 2011. Inhibition of RIG-I-mediated signaling by Kaposi's sarcoma-associated herpesvirus-encoded deubiquitinase ORF64. *J Virol* 85:10899–10904. <https://doi.org/10.1128/JVI.00690-11>.
44. Benfield CT, Mansur DS, McCoy LE, Ferguson BJ, Bahar MW, Oldring AP, Grimes JM, Stuart DI, Graham SC, Smith GL. 2011. Mapping the IkappaB kinase beta (IKKbeta)-binding interface of the B14 protein, a vaccinia virus inhibitor of IKKbeta-mediated activation of nuclear factor kappaB. *J Biol Chem* 286:20727–20735. <https://doi.org/10.1074/jbc.M111.231381>.
45. Chen RA, Ryzhakov G, Cooray S, Randow F, Smith GL. 2008. Inhibition of IkappaB kinase by vaccinia virus virulence factor B14. *PLoS Pathog* 4:e22. <https://doi.org/10.1371/journal.ppat.0040022>.
46. Graham SC, Bahar MW, Cooray S, Chen RA, Whalen DM, Abrescia NG, Alderton D, Owens RJ, Stuart DI, Smith GL, Grimes JM. 2008. Vaccinia virus proteins A52 and B14 share a Bcl-2-like fold but have evolved to inhibit NF-kappaB rather than apoptosis. *PLoS Pathog* 4:e1000128. <https://doi.org/10.1371/journal.ppat.1000128>.
47. Tang Q, Chakraborty S, Xu G. 2018. Mechanism of vaccinia viral protein B14-mediated inhibition of IkappaB kinase beta activation. *J Biol Chem* 293:10344–10352. <https://doi.org/10.1074/jbc.RA118.002817>.
48. Mathers C, Schafer X, Martinez-Sobrido L, Munger J. 2014. The human cytomegalovirus UL26 protein antagonizes NF-kappaB activation. *J Virol* 88:14289–14300. <https://doi.org/10.1128/JVI.02552-14>.
49. Gao S, Song L, Li J, Zhang Z, Peng H, Jiang W, Wang Q, Kang T, Chen S, Huang W. 2012. Influenza A virus-encoded NS1 virulence factor protein inhibits innate immune response by targeting IKK. *Cell Microbiol* 14:1849–1866. <https://doi.org/10.1111/cmi.12005>.
50. Wang K, Ni L, Wang S, Zheng C. 2014. Herpes simplex virus 1 protein kinase US3 hyperphosphorylates p65/RelA and dampens NF-kappaB activation. *J Virol* 88:7941–7951. <https://doi.org/10.1128/JVI.03394-13>.
51. Ye J, Chen Z, Li Y, Zhao Z, He W, Zohaib A, Song Y, Deng C, Zhang B, Chen H, Cao S. 2017. Japanese encephalitis virus NS5 inhibits type I interferon (IFN) production by blocking the nuclear translocation of IFN regulatory factor 3 and NF-kappaB. *J Virol* 91:e00039-17. <https://doi.org/10.1128/JVI.00039-17>.
52. Taylor SL, Frias-Staheli N, Garcia-Sastre A, Schmaljohn CS. 2009. Hantaan virus nucleocapsid protein binds to importin alpha proteins and inhibits tumor necrosis factor alpha-induced activation of nuclear factor kappa B. *J Virol* 83:1271–1279. <https://doi.org/10.1128/JVI.00986-08>.
53. Mansur DS, Maluquer de Motes C, Unterholzner L, Sumner RP, Ferguson BJ, Ren H, Strnadova P, Bowie AG, Smith GL. 2013. Poxvirus targeting of E3 ligase beta-TrCP by molecular mimicry: a mechanism to inhibit NF-kappaB activation and promote immune evasion and virulence. *PLoS Pathog* 9:e1003183. <https://doi.org/10.1371/journal.ppat.1003183>.
54. Hiscott J, Kwon H, Genin P. 2001. Hostile takeovers: viral appropriation of the NF-kappaB pathway. *J Clin Invest* 107:143–151. <https://doi.org/10.1172/JCI11918>.
55. Bachu M, Yalla S, Asokan M, Verma A, Neogi U, Sharma S, Murali RV, Mukthey AB, Bhatt R, Chatterjee S, Rajan RE, Cheedarla N, Yadavalli VS, Mahadevan A, Shankar SK, Rajagopalan N, Shet A, Saravanan S, Balakrishnan P, Solomon S, Vajpayee M, Satish KS, Kundu TK, Jeang KT, Ranga U. 2012. Multiple NF-kappaB sites in HIV-1 subtype C long terminal repeat confer superior magnitude of transcription and thereby the enhanced viral predominance. *J Biol Chem* 287:44714–44735. <https://doi.org/10.1074/jbc.M112.397158>.
56. Fiume G, Vecchio E, De Laurentis A, Trimboli F, Palmieri C, Pisano A, Falcone C, Pontoriero M, Rossi A, Scialdone A, Fasanella Masci F, Scala G, Quinto I. 2012. Human immunodeficiency virus-1 Tat activates NF-kappaB via physical interaction with IkappaB-alpha and p65. *Nucleic Acids Res* 40:3548–3562. <https://doi.org/10.1093/nar/gkr1224>.
57. Ehrhardt C, Ruckle A, Hrinčius ER, Haasbach E, Anhlan D, Ahmann K, Banning C, Reiling SJ, Kuhn J, Strobl S, Vitt D, Leban J, Planz O, Ludwig S. 2013. The NF-kappaB inhibitor SC75741 efficiently blocks influenza virus propagation and confers a high barrier for development of viral resistance. *Cell Microbiol* 15:1198–1211. <https://doi.org/10.1111/cmi.12108>.
58. Mazur I, Wurzer WJ, Ehrhardt C, Pleschka S, Puthavathana P, Silberzahn T, Wolff T, Planz O, Ludwig S. 2007. Acetylsalicylic acid (ASA) blocks influenza virus propagation via its NF-kappaB-inhibiting activity. *Cell Microbiol* 9:1683–1694. <https://doi.org/10.1111/j.1462-5822.2007.00902.x>.
59. Nimmerjahn F, Dudziak D, Dirmeier U, Hobom G, Riedel A, Schlee M, Staudt LM, Rosenwald A, Behrends U, Bornkamm GW, Mautner J. 2004. Active NF-kappaB signalling is a prerequisite for influenza virus infection. *J Gen Virol* 85:2347–2356. <https://doi.org/10.1099/vir.0.79958-0>.
60. Wurzer WJ, Ehrhardt C, Pleschka S, Berberich-Siebelt F, Wolff T, Walczak H, Planz O, Ludwig S. 2004. NF-kappaB-dependent induction of tumor necrosis factor-related apoptosis-inducing ligand (TRAIL) and Fas/FasL is crucial for efficient influenza virus propagation. *J Biol Chem* 279:30931–30937. <https://doi.org/10.1074/jbc.M403258200>.
61. Pinto R, Herold S, Cakarova L, Hoegner K, Lohmeyer J, Planz O, Pleschka S. 2011. Inhibition of influenza virus-induced NF-kappaB and Raf/MEK/ERK activation can reduce both virus titers and cytokine expression simultaneously in vitro and in vivo. *Antiviral Res* 92:45–56. <https://doi.org/10.1016/j.antiviral.2011.05.009>.
62. Hoagland DA, Moller R, Uhl SA, Oishi K, Frere J, Golyner I, Horiuchi S, Panis M, Blanco-Melo D, Sachs D, Arkun K, Lim JK, tenOever BR. 2021. Leveraging the antiviral type I interferon system as a first line of defense against SARS-CoV-2 pathogenicity. *Immunity* 54:557–570. <https://doi.org/10.1016/j.immuni.2021.01.017>.
63. Monk PD, Marsden RJ, Tear VJ, Brookes J, Batten TN, Mankowski M, Gabbay FJ, Davies DE, Holgate ST, Ho LP, Clark T, Djukanovic R, Wilkinson TMA, Inhaled Interferon Beta COVID-19 Study Group. 2021. Safety and efficacy of inhaled nebulised interferon beta-1a (SNG001) for treatment of SARS-CoV-2 infection: a randomised, double-blind, placebo-controlled, phase 2 trial. *Lancet Respir Med* 9:196–206. [https://doi.org/10.1016/S2213-2600\(20\)30511-7](https://doi.org/10.1016/S2213-2600(20)30511-7).
64. Oguntuyo KY, Stevens CS, Hung CT, Ikegame S, Acklin JA, Kowdle SS, Carmichael JC, Chiu HP, Azarm KD, Haas GD, Amanat F, Klingler J, Baine I, Arinsburg S, Bandres JC, Siddiquey MNA, Schilke RM, Woolard MD, Zhang H, Consortium CA, Duty AJ, Kraus TA, Moran TM, Tortorella D, Lim JK, Gamarnik AV, Hioe CE, Zolla-Pazner S, Ivanov SS, Kamil JP, Krammer F, Lee B, COVIDAR Argentina Consortium. 2021. Quantifying absolute neutralization titers against SARS-CoV-2 by a standardized virus neutralization assay allows for cross-cohort comparisons of COVID-19 sera. *mBio* 12:e02492-20. <https://doi.org/10.1128/mBio.02492-20>.
65. Love MI, Huber W, Anders S. 2014. Moderated estimation of fold change and dispersion for RNA-seq data with DESeq2. *Genome Biol* 15:550. <https://doi.org/10.1186/s13059-014-0550-8>.
66. Anonymous. 2016. ggplot2: elegant graphics for data analysis. Springer, Cham, Switzerland.
67. Liberzon A, Birger C, Thorvaldsdottir H, Ghandi M, Mesirov JP, Tamayo P. 2015. The Molecular Signatures Database (MSigDB) hallmark gene set collection. *Cell Syst* 1:417–425. <https://doi.org/10.1016/j.cels.2015.12.004>.
68. Langmead B, Salzberg SL. 2012. Fast gapped-read alignment with Bowtie 2. *Nat Methods* 9:357–359. <https://doi.org/10.1038/nmeth.1923>.
69. Buenrostro JD, Giresi PG, Zaba LC, Chang HY, Greenleaf WJ. 2013. Transposition of native chromatin for fast and sensitive epigenomic profiling of open chromatin, DNA-binding proteins and nucleosome position. *Nat Methods* 10:1213–1218. <https://doi.org/10.1038/nmeth.2688>.
70. Robinson MD, McCarthy DJ, Smyth GK. 2010. edgeR: a Bioconductor package for differential expression analysis of digital gene expression data. *Bioinformatics* 26:139–140. <https://doi.org/10.1093/bioinformatics/btp616>.
71. Soneson C, Robinson MD. 2018. Bias, robustness and scalability in single-cell differential expression analysis. *Nat Methods* 15:255–261. <https://doi.org/10.1038/nmeth.4612>.
72. Wu D, Smyth GK. 2012. Camera: a competitive gene set test accounting for inter-gene correlation. *Nucleic Acids Res* 40:e133. <https://doi.org/10.1093/nar/gks461>.